A&A, 709, A180 (2026)
https://doi.org/10.1051/0004-6361/202658909

Astronomy & Astrophysics

eROSITA's cool star population explained

J. H. M. M. Schmitt*, P. C. Schneider, S. Czesla, S. Freund, and J. Robrade

Hamburger Sternwarte, Universität Hamburg, Gojenbergsweg 112, 21029 Hamburg, Germany

Received 9 January 2026 / Accepted 25 March 2026

ABSTRACT

The rotation-activity connection is the standard paradigm for interpreting chromospheric and coronal activity in late-type stars, namely, stars with outer convection zones. This paradigm states that activity increases with decreasing rotation period until a saturation limit is reached. By scaling rotation periods with the convective turnover time via the Rossby number, Ro, saturation is expected to occur at a universal value across all spectral types. In our paper, we systematically investigate the relationship between rotation and activity as measured though X-ray emission for a large sample of late-type stars to test the universal applicability of this paradigm. To this end, we utilized TESS short-cadence space photometry to determine the rotation periods for late-type stars identified in the eROSITA all-sky survey. This combined dataset provides rotation and X-ray measurements for 14 004 stars, representing a sample size increase of more than an order of magnitude compared to previous studies. Our results show that F-type stars do not reach the "classical" saturation limit of $L_X/L_{bol} \approx 10^{-3}$, instead exhibiting significantly lower L_X/L_{bol} values. We find that the convective turnover times derived from this sample closely agree with theoretical computations, supporting the idea that Rossby number-activity relations hold for all late-type main sequence stars. The lower level of activity in earlier spectral types (e.g., F-type and late A-type stars) is a physical consequence of their short convective turnover times, which prevent them from rotating rapidly enough to ever reach the saturation regime. We demonstrate that a simple model incorporating our derived turnover times versus color can successfully reproduce the observed characteristics of the eROSITA X-ray activity distribution, as measured by the L_X/L_{bol} ratio and *Gaia* BP-RP color.

Key words. stars: activity – stars: coronae – stars: general – stars: late-type – stars: rotation – stars: statistics

1. Introduction

The most fundamental stellar parameter controlling the activity level of a given late-type star is its rotation rate. This leads to the rotation-activity paradigm, which roughly states that rapid rotators are the most "active" stars with the largest surface coverage of star spots and the highest levels of chromospheric and coronal emission. In this paper, we are concerned with photospheric modulations caused by star spots, which are used to provide estimates of stellar rotation periods as well as with coronal emissions observed at X-ray wavelengths. Following the pioneering study of Pallavicini et al. (1981), numerous studies of the relation between X-ray emission and rotation periods of stars have been carried out; a recent review of this topic is provided by Santos et al. (2024). These studies have contributed towards making the rotation-activity paradigm the commonly accepted standard framework to discuss and interpret all magnetic "activity" phenomena observed in late-type stars. It is important to keep in mind that "activity" phenomena in late-type stars comprise a plethora of different observational findings observed at different wavelength ranges and typically referring to different parts of the outer atmospheres of the underlying stars; for a recent review, we refer to the textbook by Basri (2021).

Star spots are among the best tools presently at our disposal to determine the rotation period of a given star. To the extent that the star spots are sufficiently inhomogeneously distributed on the stellar surface and "live" sufficiently long, the periodic signatures in the resulting stellar light curves are directly related to the sought for stellar rotation period. Needless to say, nature can be unkind at times and we refer to Basri & Shah (2020) for an in-depth study of the information content of photometric light curves. The availability of space-based high-precision photometry has overcome the severe limitations of ground-based photometry in terms of temporal coverage and photometric precision; for example, using data from the *Kepler* satellite, McQuillan et al. (2014) were able to measure periods for more than 34 000 stars. Yet, as was made apparent by the detailed mission description by Borucki et al. (2010), the sky area covered by the *Kepler* satellite was limited and the target stars are usually too faint to be detectable as X-ray sources even in deep X-ray pointings.

Stellar coronae can be best diagnosed in the X-ray range; since stellar photospheres are X-ray dark, an X-ray flux measurement provides a direct measure of the coronal emission strength of a given star. Thanks to eROSITA's all-sky survey (Merloni et al. 2024) the number of known X-ray sources and in particular X-ray emitting stars has increased tremendously in recent years. Already the first half year of eROSITA's all-sky survey (Merloni et al. 2024) has provided ≈1.3 million X-ray sources detected in the 0.2–2.3 keV energy band (Merloni et al. 2024), and more than 100 000 of these X-ray sources can be identified with so-called normal stars, the majority being cool dwarf stars (Freund et al. 2024). Since X-ray surveys tend to focus on the more X-ray luminous active stars, according to the rotation-activity paradigm, we would expect the underlying population of X-ray-detected stars to consist of predominantly rapid rotators.

Thus, it is clear that to understand the population of cool stars associated with eROSITA X-ray sources, we need rotation periods for many thousands of stars distributed over the sky, with the expectation that many of these periods are rather short and the X-ray emission is at or close to the saturation limit. As shown by Freund et al. (2024), the majority of the expected stellar counterpart population is (by comparison) optically bright

* Corresponding author: jschmitt@hs.uni-hamburg.de

(i.e., brighter than 13–15 in the *Gaia* G-band, depending on spectral type). A valuable source for rotation periods of such stars is provided by the Transiting Exoplanet Survey Satellite (TESS) mission, which provides short-cadence photometry over the whole sky for brighter stars Ricker et al. (2015) and it is therefore close to ideal to be used in conjunction with the eROSITA X-ray all-sky survey. By combining eROSITA and TESS, we ought to be able to extract such data for many thousands of stars. At the same time, accurate *Gaia* photometry is available for almost all our sample stars, allowing for a precise placement of the stars in a color-magnitude diagram and obtaining an estimate of stellar mass for main sequence (MS) objects.

The other important quantities that are useful for characterizing the activity of late-type stellar X-ray sources is the convective turnover time. Noyes et al. (1984) were the first to introduce the Rossby number (i.e., the ratio between rotation period and convective turnover time) into the interpretation of stellar activity data. They derived a unique period-activity relationship for their sample of chromospherically active late-type MS stars and demonstrated a rather tight relationship between rotation and activity: stars with small Rossby numbers (i.e., with short rotation periods) exhibit high levels of (chromospheric) activity and vice versa; as pointed out by Noyes et al. (1984), this finding suggests an interpretation in terms of dynamo related activity since simple scaling relations yield a dependence of $N_D \sim R_o^{-2}$, with N_D being the dynamo number, characterizing the "dynamo strength". The approach of Noyes et al. (1984) was carried into the X-ray range by Pizzolato et al. (2003) and Wright et al. (2011). They considered how, for example, the X-ray luminosity, L_X, or the fractional X-ray luminosity, L_X/L_{bol}, depend on rotation, using stellar samples with known X-ray properties and rotation periods. In the X-ray range, Wright et al. (2011) found X-ray "saturation" at a level of $L_X/L_{bol} \approx 10^{-3}$ for Rossby numbers below 0.13, while for larger Rossby numbers (i.e., slower rotators), the L_X/L_{bol} ratio decreases rapidly with an increasing Rossby number.

The convective turnover time determinations by Noyes et al. (1984), Pizzolato et al. (2003), and Wright et al. (2011) were all entirely empirical; whereas, in contrast, Landin et al. (2010) and more recently Landin et al. (2023) published theoretical estimates of convective turnover times for cool stars. Specifically, Landin et al. (2023) published convective turnover times for stars covering the mass range 0.1–1.5 $M_\odot$ for various evolutionary stages. In particular, these authors produced both global convective turnover times defined as the means over the whole stellar convection zone, along with local convective turnover times computed at half a mixing length above the base of the convection zone; we refer to Sects. 3.1 and 3.2 of Landin et al. (2023) for details. As Landin et al. (2023) have shown, there is reasonably good agreement between the empirical and theoretical values for convective turnover time; hence, the introduction of the Rossby number appears to be a sound concept.

The purpose of this paper is to analyze the available TESS short-cadence data for those sources identified with coronal emitters from the eROSITA all-sky survey to derive their periods, whenever possible. To focus our paper on the physical results, we moved all sections primarily concerned with technicalities into the appendices. We provide on a brief overview of the adopted procedures in Sect. 2, while the bulk of our paper deals with the derived results and their interpretation. The specific plan of our paper is as follows. In Sect. 2 we first provide a brief overview of our TESS period determinations, while the more technical details of our work are presented in Appendices A and B. The resulting periods are also presented in Sect. 2, as well as a comparison with other period determination efforts, and we also give the statistics and reliability of our period determinations in comparison. The astrophysical results of our work are presented in Sect. 3, where we describe the construction of our reference stellar sample. We also present color-magnitude diagrams of the stellar sources and study the dependence of activity on rotation periods. We introduce the Rossby numbers and derive the convective turnover times from our stellar sample. We show that rapidly rotating stars of spectral type F6 or earlier cannot reach the saturation regime. Finally, we present a simple toy model that describes the X-ray activity of eROSITA's cool star population as a function of color.

2. TESS rotation periods of eROSITA detected coronal sources

In this paper, we consider X-ray sources extracted from the 1.3 million X-ray sources detected in the 0.2–2.3 keV energy band during the first half year of eROSITA's all-sky survey (Merloni et al. 2024). Specifically, we used our HamStar algorithm (Freund et al. 2024) to identify stellar (coronal) sources. In brief, HamStar uses information from *Gaia* DR3 (Gaia Collaboration 2023) and Tycho (Høg et al. 2000) to calculate the probability, $p_{stellar}$, that a given eROSITA X-ray source is actually a coronal X-ray emitter and we refer to Freund et al. (2024) for a detailed account of the adopted identification procedures. For our study, we consider all eRASS1 sources with $p_{stellar} > 0.5$ and a *Gaia* DR3 ID as an identification. The so-called TESS input catalog (TIC; Paegert et al. 2022) provides *Gaia* DR2 IDs for most sources and we mapped the *Gaia* DR3 IDs from HamStar to *Gaia* DR2 IDs using the `dr2neighbourhood` table available as part of *Gaia* DR3[1]. In this way, the high probability stellar eROSITA X-ray sources were associated with a TIC ID using this *Gaia* DR2 ID and a total of about 69 000 sources resulted from this procedure.

The primary scientific goal of the TESS mission is the detection of exoplanets around the brighter stars by performing differential photometry with a cadence of two minutes simultaneously, utilizing its four red-band wide-field cameras that cover a 24° × 96° strip on the sky for a total 27 days (denoted as "sector" in the TESS terminology). A detailed description of the TESS mission is given by Ricker et al. (2015). We checked which sources had been observed by TESS in short-cadence mode in sectors 1–58, downloaded the respective data from the TESS-MAST archive, and analyzed the data following the procedures described in Appendix B. In addition to the *Gaia* data, HamStar also incorporates information from Tycho and some eROSITA sources, mainly the optically brighter ones, currently have only a Tycho but no *Gaia* counterpart. For those sources, we found that matching based on Tycho ID left many sources without a reasonable TIC counterpart and we opted for a distance based matching for those sources, which added 375 sources to our input catalog. Thus, in total, we obtained 69 179 eRASS1 sources in the German half of the eROSITA sky brighter than G = 13 and contained in the TESS input catalog.

The TESS data of a given source do not come as a contiguous data stream even in a single TESS sector; rather the data stream is interrupted, usually after about 13 days, when the data taken during one TESS orbit is downloaded to the ground. Furthermore, the TESS data for a given object might show pronounced jumps

[1] Some of our sources have more than one possible DR2 counterpart. In those cases, we selected the one closest in magnitude to the DR3 value.

between the first data segment in a given sector and the second segment, which is clearly instrumental. These gaps and instrumental effects obviously are a challenge for the data analysis. In addition, the coverage of sources with respect to TESS sectors is quite inhomogeneous. Sources near the ecliptic poles receive a lot of exposure, those near the ecliptic equator much less, while periods derived in different sectors may agree or disagree and, thus, a special treatment is required.

Measuring a period in a noisy data set can be quite cumbersome. To reduce possibly incorrect determinations of periods we used three different procedures to assess whether significant periodicity is contained in a given data set. Specifically, we use the generalized Lomb-Scargle (GLS) analysis, as developed by Ferraz-Mello (1981) and Zechmeister & Kürster (2009), the autocorrelation function of the light curve data following the approach by McQuillan et al. (2014), and the phase dispersion minimization procedure developed by Stellingwerf (1978). These three methods measure somewhat different properties of the analyzed data stream: the GLS analysis attempts to identify the most significant Fourier components in the data, the autocorrelation approach investigates the correlation properties of the data, and the phase dispersion minimization seeks those periods which result in the "best" light curves in the sense that the folded data show the least amount of dispersion around some "mean" light curve.

The rotational signals in these eROSITA-selected TESS sources are typically not produced by eclipses (although we do find a fair number of eclipsing binaries in our sample); rather, they are produced by star spots inhomogeneously distributed on the stellar surface. However, star spots come and go, their surface distribution changes (maybe all the time); furthermore, the stars may rotate differentially, thus all these effects may change the rotational signatures in the data. On the other hand, the light changes in an eclipsing binary are very regular, except that the surfaces of such stars are often also covered by time variable spots.

2.1. Period determination: Overview

In this section, we provide an overview of our period determination scheme, with more detail found in Appendix B. The TESS data downloaded from the TESS-MAST archive contain two types of light curve files: one with fluxes based on Simple Aperture Photometry (SAP) and one with fluxes based on pre-search data conditioning SAP (PDCSAP). The PDCSAP algorithm attempts to identify and correct for systematic instrumental trends in the TESS light curves and is geared towards transit detection; for a detailed discussion of the applied procedures, we refer to Jenkins et al. (2016). However, we found TESS light curves where an obvious overcorrection was performed by the PDCSAP procedures. An example is shown in Fig. 1, which shows the SAP and PCDSAP light curves in comparison for the case of TIC 270771392 observed in sector 34. We note that only the modulated part of the light curve is shown and a constant has been subtracted. As can be seen from Fig. 1, the two light curves agree well in the time range of 3–10 days and 14–16 days, yet the start and end of the first observing interval and the features near days 16–18 and day 23 until the end of the observations are quite different and actually lead to incorrect period estimates. In the specific case of TIC 270771392, another light curve was obtained in sector 8, which suggests that the SAP values are much closer to the truth than the PDCSAP values; other examples of apparent overcorrections by the PDCSAP procedure are given by Hedges et al. (2021).

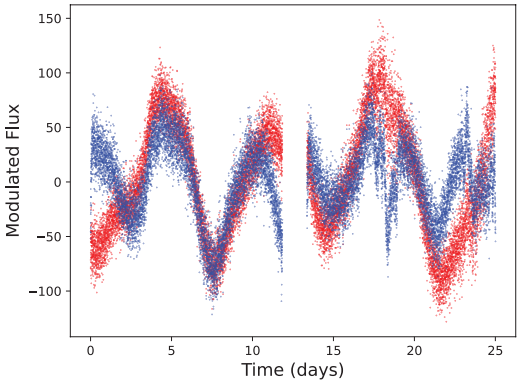

Fig. 1. Comparison of TESS SAP light curve (red data points) and TESS PDCSAP (blue data points) for the source TIC 270771392 observed in sector 34; see text for details.

We therefore decided to work with SAP fluxes and applied only some moderate light curve corrections: sectors with more than one data gap of one day or more were ignored altogether to avoid additional light curve aliasing, while the data in the two sectors halves were adjusted to the same mean to avoid long-term trends. Finally, we computed the dispersion σ of the light curve and rejected all data with deviations of more than three σ to reduce the influences of systematic trends that are often seen at the beginning or end of TESS sectors. It is clear that we do not claim to have removed all instrumental effects from the light curves and from our results (presented in Sect. 3.1) and some instrumental effects will affect these periods.

To deal with all these effects, we devised a special treatment of the derivation of TESS rotation periods. Our period determination scheme is primarily based on the Lomb-Scargle periodogram power (GLS; as defined by Zechmeister & Kürster 2009); however, we also considered phase dispersion minimization and/or autocorrelation to finally arrive at a period assignment for every X-ray source; a detailed account of the adopted procedures is given in Appendices B.1 and B.2. To indicate our confidence in these period assignments we introduced an empirical quality grading scheme ranging from grades 1–7. A period grade of 4 requires a consistent period determination of the data in a given sector (to within 10%) with three different period searching methods. If successful and consistent period measurements are available in more than a single sector, the assigned period quality grade is increased by one, if at least three consistent period measurements in different sectors are available, by 2 and so on. The maximally possible grade is 7, implying that there are at least nine consistent high quality period measurements available for the given source. A more detailed description of this procedure is given in Appendix B.3, where we also provide a table with the derived grade frequency distribution. For 14 004 sources, we managed to obtain valid period measurements with grades 3 and larger, whereby 11 731 of the derived periods have quality assignments greater than 3. That does not imply that the periods for the remaining 2273 sources are wrong; however, the rate of incorrect period determinations among these sources is expected to be higher.

An exemplary listing of our period results is given in Table 1, the full table is available in the online material. In Table 1, we provide the respective TIC-ID numbers, the derived periods and their errors (whenever available) The flag MS denotes MS stars, the flag PB indicates a "possibly bad" period, namely, where we suspect it is not a rotation period of the target object. For more details, we refer to Sect. 3.1.

Table 1. Successful period determinations (extract).

TIC-ID	Period (day)	Period error (day)	Grade	MS flag	PB flag
102723	4.05	0	4	1	0
113645	12.79	0	4	1	0
120016	0.16	0	4	1	0
122797	7.39	0	4	0	0
138893	15.13	0	4	1	0
141778	3.44	0	4	1	0
155455	3.17	0	3	0	0
167121	10.35	0	4	1	0
592590	8.35	0	4	1	0
593228	14.76	0.23	5	1	0
610232	4.98	0	4	1	0
614576	14.91	0	4	1	0
615133	0.86	0	4	1	0
665581	0.24	0	4	1	0
671564	0.19	0	4	1	0
672624	0.56	0	4	1	0
675445	10.72	0	4	0	0
710947	9.05	0	4	1	0
737327	1.62	0	5	1	0
768859	8.85	0.44	5	1	0
775434	5.64	0.02	5	1	0
862763	1.01	0	3	1	0
864120	8.10	0	4	1	0
864246	7.67	0	4	1	0
864738	1.46	0	3	1	0
893123	8.77	0	4	1	0
990827	10.30	0.21	5	1	0
990903	8.03	0.29	5	0	0

Notes. The full table is available at the CDS. Col. 1 gives TIC ID number. Col. 2 the derived period. Col. 3 indicates its error. Col. 4 provides the quality flag. Cols. 5 and 6 give the MS flag (i.e., objects in the red polygonal area in Fig. 6) and PB flag (i.e., bad period objects inside green dashed area in Fig. 7). We note that a period error is computed only for sources with successful period determinations in at least two sectors.

2.2. Comparison with other period determinations

We first compare our new period determinations with other period determination efforts and check to what extent the different applied methodologies agree or disagree. For this sanity check, we used the rotation modulation studies of *Gaia* sources published by Distefano et al. (2023); the study of the relation of X-ray activity and rotation for cool stars by Wright et al. (2011), who used a variety of ground-based rotation measurements for 824 known X-ray sources associated with cool stars; the results of Prša et al. (2022), who presented a catalog of 4584 eclipsing binaries detected in TESS short-cadence observations; and the study by Mowlavi et al. (2023), who presented a catalog of more than 500 000 eclipsing binary candidates based on *Gaia* data. Finally, we compared our periods to those produced using the SpinSpotter code developed by Holcomb et al. (2022).

2.2.1. Comparison with *Gaia* periods

Using the brightness measurements of the various focal plane transits observed during the *Gaia* mission, Distefano et al. (2023) analyzed the observed variations and present

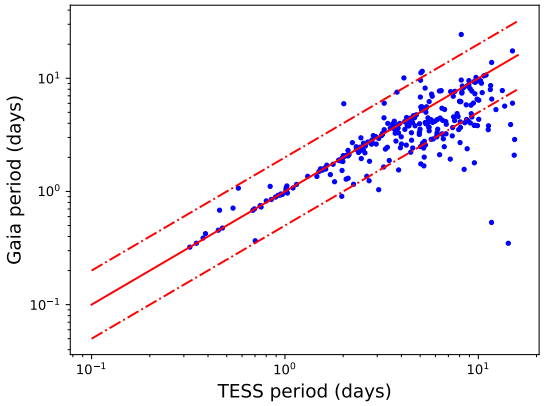

Fig. 2. Comparison of TESS periods as derived in this paper and *Gaia* periods as derived by Distefano et al. (2023) for 275 objects with eROSITA detections. Solid line indicates consistent period determinations, dash/dotted lines indicate a period ratio of 2 and 1/2; see text for details.

determinations of rotation modulation for about 474 000 *Gaia* DR3 late-type stars. Due to the complex *Gaia* scanning law, the sampling properties and the completeness of this sample vary considerably over the sky. Distefano et al. (2023) argued that the detection of rotation periods below about five days is favored and estimated that about 70–80% of the detected periods are correct. Upon inspecting the brightness distribution of those sources with reported periods, we find that most of these stars are below the TESS brightness limit; however, a small fraction of 275 objects has an eROSITA detected counterpart and a TESS light curve with a successful period measurement with grade 4 or better.

In Fig. 2, we compare "our" TESS period measurements obtained from TESS data (as described above) to the periods determined from *Gaia* data as reported by Distefano et al. (2023). In Fig. 2, the red solid line indicates period equality, while the dashed lines indicated aliases by factors of 1/2 and 2. We specifically find 129 sources with a period agreement of better than 15% and another 38 sources where the *Gaia* period is twice the TESS period, which could be explained by an alias of the TESS period measurement.

We checked the largest two outliers (with the TESS period above 10 d, and *Gaia* period below 1 d). In the case of TIC 139285669, we conclude that the TESS period of 14.3 d is instrumental; the *Gaia* period of 0.35 d is present in the TESS data as well; however it is above our cutoff of 0.1 in GLS power only in one of three sectors. Similar considerations apply to TIC 459944057, which was observed only in one sector; the *Gaia* period of 0.53 d is clearly present in the TESS data (but below our chosen cutoff) and the long period is of instrumental origin.

2.2.2. Comparison with periods derived by Wright et al. (2011)

Wright et al. (2011) present a study of non-simultaneous X-ray and rotation measurements of 824 cool stars with an emphasis on the rotation-activity relation and its dependence on spectral type. The rotation measurements presented by Wright et al. (2011) cover periods between about 0.2 up to 40 d (i.e., a period range not covered by our analysis). Obviously, the long-period systems are expected to exhibit lower X-ray activity and are therefore not expected to show up in shallower all-sky surveys. Again considering only matches with grade 4 or better, we find 74 matches and show the comparison between the periods measurements in

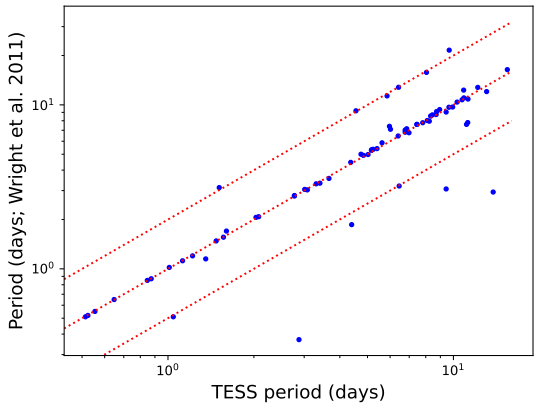

Fig. 3. Comparison between rotation periods of cool stars determined by Wright et al. (2011) and those in this paper. The unity line as well as the lines for half and twice the periods are also indicated. See text for details.

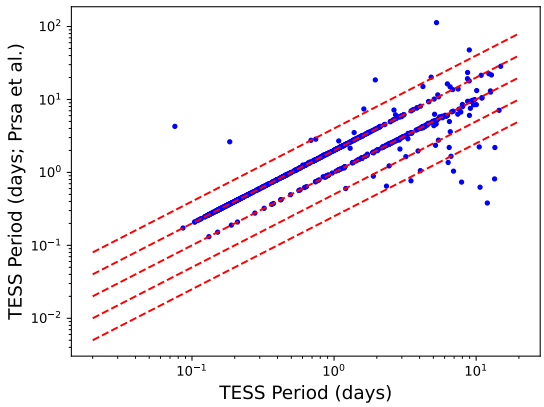

Fig. 4. Comparison of periods derived in this paper with those derived by Prša et al. (2022) for a sample of eclipsing binaries. The unity line is shown as well lines at 1/4, 1/2, 2, and 4 times the period. For details, see text.

Fig. 3. For 57 sources, the measured period ratios are within 15%, while another eight cases can be attributed to aliasing; thus, the agreement appears to be very satisfactory. There is one significant outlier due to the star TIC 455007634; an even casual inspection of the TESS data shows that the period of 0.37 d listed by Wright et al. (2011) cannot possibly be correct.

2.2.3. Comparison with periods derived by Prša et al. (2022)

Prša et al. (2022) present a catalog 4584 eclipsing binaries identified in TESS sectors 1–26 in the basis of short-cadence observations. For a detailed description of the detection and validation procedures, we refer to the discussions in Prša et al. (2022).

Among the eclipsing binaries cataloged by Prša et al. (2022), we find an eROSITA X-ray source with a TESS period for more than 706 entries and show the comparison in Fig. 4. For 163 entries, the periods agree within 15%; for 494 entries., Prša et al. (2022) found twice our period (to within 15%); and for eight sources, it is the other way around. Thus, if we include the aliased sources, the agreement is very good, however, it is also very clear that for eclipsing binaries the bias, for example demonstrated in Fig. A.1, is very important and Fig. 4 suggests that our procedure, which is based on GLS periodograms and not optimized for eclipsing binaries, has a strong tendency to pick up half the binary period which is not surprising.

2.2.4. Comparison with periods derived by Mowlavi et al. (2023)

Mowlavi et al. (2023) present a catalog of more than 500 000 eclipsing binary candidates based on *Gaia* photometry. Again, many of these sources are quite faint and therefore out of the reach of both TESS and eROSITA. Nevertheless we find a match for 622 of these sources and show a period comparison in Fig. 5. We note that in this case the origin of the data for the period determinations are different, namely, TESS for "our" periods and *Gaia* for those presented by Mowlavi et al. (2023).

A detailed examination shows that the period ratios agree to within 15% in 63 cases, while in 498 cases, we find half the period (to within 15%) of those derived by Mowlavi et al. (2023) and in 3 cases, it is the opposite case. Thus, including aliased periods the agreement again is satisfactory, but again, as is the

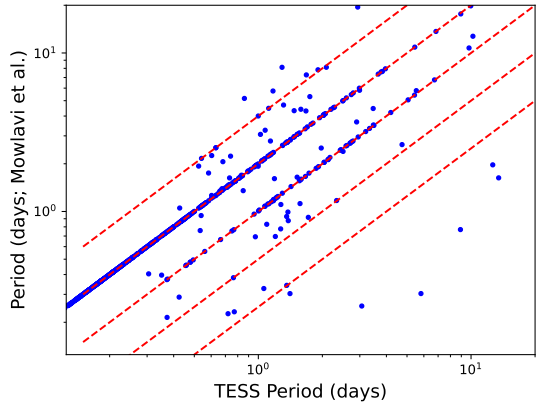

Fig. 5. Comparison of periods derived in this paper with those derived by Mowlavi et al. (2023) for a sample of eclipsing binaries. The unity line is shown as well lines at 1/4, 1/2, 2 and 4 times the period; for details see text.

case for the sample presented by Prša et al. (2022), the tendency for GLS to pick up half the binary period is very obvious.

We specifically checked a data point which yielded a large TESS period (3.06 d) and small *Gaia* period (0.25 d), which refers to the star TIC 142742998 (=BD-03 2599), a known, but little studied spectroscopic binary of spectral type G8e; the TESS light curve shows two eclipses and a photometric modulation with a period of slightly over 3 days. Therefore, we are very confident that "our" TESS period is correct.

2.2.5. Comparison with periods derived by Holcomb et al. (2022)

Using TESS data, Holcomb et al. (2022) derived periods for 13 504 stars out of a sample of 136 868 objects with their SpinSpotter code, a period search code based on autocorrelation analysis. Unfortunately, the results of Holcomb et al. (2022) are not publicly available, yet the SpinSpotter code is. To compare to our results, we used the SpinSpotter code on the SAP fluxes – noting that Holcomb et al. (2022) used PDCSAP fluxes – for 946 stars with TESS data available for two or more sectors, periods of less than 20 days, and a relative dispersion of less than 0.3. In this sample, 85.5% of the objects have the same period, whereas in 5.8% of the cases, the SpinSpotter periods are twice as large

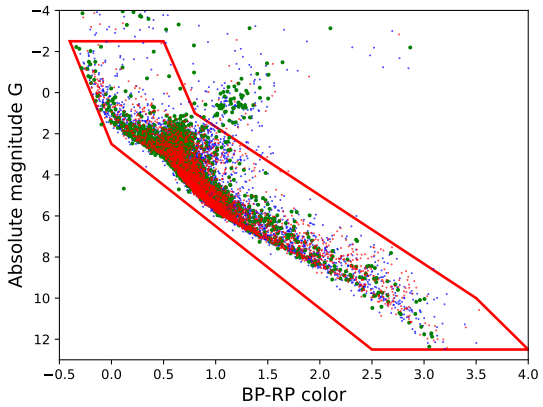

Fig. 6. Color magnitude diagram (based on *Gaia* values) for eROSITA detected stars with successful TESS period measurements, with the indicated red polygonal region defining our MS sample. The data points are color coded according to period quality: green (grade 3), blue (grade 4), and red for higher grades. See text for details.

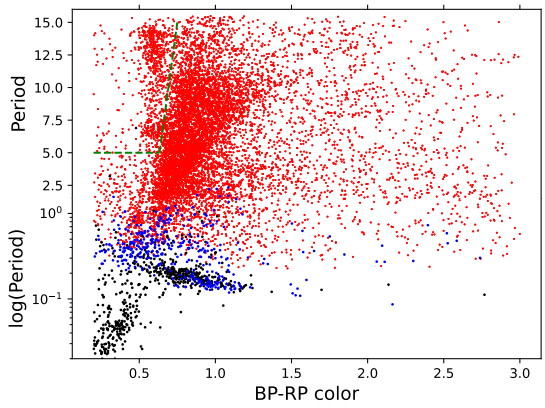

Fig. 7. Period (in days) vs. BP-RP color for the MS sample with grade 4 and higher; black symbols refer to stars with periods in excess of the estimated break-up period, blue symbols refer to stars with more than 50% of breakup, red symbols to those below. Note: the period scale for periods below 1.5 d is logarithmic. The periods for the stars inside the green dashed lines are not thought to be rotational periods. See text for details.

and in 0.7% of the cases, the opposite is the case. Thus, if we include the aliased periods, we can find an agreement in more than 90% of the cases considered.

2.2.6. Summary of period comparisons

Overall, we consider the agreement between previously derived periods and our new TESS-based periods more than satisfactory. It is clear that in the case of eclipsing binaries our GLS-based period determination has a considerable probability to pick up only half the period similar to the case of an active star with two centers of activity on opposing hemispheres. There is (as usual) the problem of aliasing, which is difficult to ascertain in a statistical way. It is clear that some of our TESS periods are of instrumental nature in particular those near about 13 days; however, the comparison with other period determination efforts that do not suffer from this 13-day bias inherent in the TESS data shows that in quite a few cases, our long periods (i.e., even in the vicinity of 13 days) are accurate.

3. Results and discussion

3.1. Construction of a stellar sample

With our period measurements, we proceeded to construct a well-defined stellar sample for all our further investigations. To this end, we placed the X-ray sources with successful period measurements into a the color-magnitude diagram. Also, we had to take into account optical contamination. As discussed by Schmitt et al. (2022), the eROSITA signals for brighter objects can be corrupted by optical light and not be due to X-ray radiation. To assess the possible level of optically induced X-ray flux, we used the expression derived by Schmitt et al. (2022) to compute an expected optical contamination rate, c_{opt}, and demand that the actually measured rate, c_X, exceeds c_{opt} by at least a factor of 5.

In Fig. 6 we show a color-magnitude diagram of the selected sources, where we also indicate a polygonal region, which we consider to contain bona fide MS objects; objects inside the polygon are indicated with the MS flag in Table B.1. It is obvious that the vast majority of objects with accepted period measurements are indeed MS stars (10 798). Outside the polygonal region in Fig. 6, we find less than 2% of the overall population. The assigned period quality grades are color-coded in Fig. 6, the green data points are due to sources with the lowest grade (3) and appear to be clustered for giant stars. To avoid possible problems with contamination, we only considered periods with grade 4 or higher in the following.

Next, we considered the relationship between the BP-RP colors and periods for those X-ray sources associated with MS objects and successful period determinations; namely, the stars inside the red polygon in Fig. 6 and grade 4 and higher, which is shown in Fig. 7. As is apparent from Fig. 7, most of our sample stars are located in the BP-RP color range 0.5–1.0; namely, in the range of F and G type stars. We first consider the short-period regime, where we notice two specific regions: one region (1) with objects in the color range 0.0 < BP-RP < 0.5 and periods below 0.1 d with a tendency for increasing period with increasing color, and a second region (2) of sources in the color range 0.5 < BP-RP < 1.2 and periods between 0.3 d > P > 0.1 d, with a tendency of decreasing periods with increasing colors.

To interpret the short-period sources shown in Fig. 7, it is of interest to examine the break-up velocities and periods for the MS sample stars. In this context we define the break-up period, P_{br}, as

$$P_{br} = \frac{2\pi R}{v_{br}}, \tag{1}$$

with the break-up velocity, v_{br}, defined in the usual way as

$$v_{br} = \sqrt{\frac{GM}{R}}, \tag{2}$$

with M and R denoting stellar mass and radius, respectively, and G is the gravitational constant. In Fig. 7, those stars with measured periods of more than half the calculated break-up period are shown as blue and black data points and, as expected, these stars populate the short-period region in Fig. 7. For an hypothetical binary consisting of two solar-like stars in contact, we can compute a period of 0.23 d and P ~ M. Thus, we expect that the stars in region (2) are close or contact binaries, whereas the stars in region (1) are probably pulsating sources. While we would expect identical orbital and rotation periods for close binaries, it

should be clear that those periods indicated in Fig. 7 with black data should not be treated as pure rotation periods.

Finally we note a region where stars with bluish colors and periods in excess of 5 days are located, delineated by the green dashed line in Fig. 7. We can further note that there appears to be a clustering of periods near 6.5 days and 13 days. We suspect that these periods are instrumental and ignore these data points inside the green dashed line in Fig. 7 in our subsequent analysis.

3.2. Some exemplary stars of low activity

Before discussing and interpreting our eROSITA/TESS results in detail, we introduced four additional rather well known low-activity stars for purposes of comparison and checking the validity of the rotation-activity paradigm. We specifically refer to the A-type stars Altair (= α Aql) and Alderamin (= α Cep), the Sun, and Barnard's star; for these stars we have no eROSITA measurements, but X-ray flux and rotation period measurements are available from other sources.

Altair is a nearby late A-type star of spectral type A7IV-V, considered to be the "hottest magnetically active stars in X-rays" by Robrade & Schmitt (2009); these authors report on a long XMM-Newton pointing on Altair, carried out a detailed spectral analysis of the X-ray data and find an X-ray luminosity of 1.4×10^{27} erg/s and a logarithmic L_X/L_{bol} ratio of −7.4. Altair has long been known to be a very rapid rotator with v sin(i) values exceeding 200 km/s; van Belle et al. (2001) interferometrically resolved Altair and explicitly derive its oblateness due to its rapid rotation. Altair's rotation period turns out to be about 9.5 hours, and its equatorial rotation velocity amounts to a substantial fraction of its break-up velocity. Based on TESS observations of Altair, Rieutord et al. (2024) derive an age of 88 Myr based on stellar oscillations, while earlier age determinations based on isochrones described by Lachaume et al. (1999) yielded ages of about 1.2 Gyrs. Thus, Altair appears to be definitely younger than the Sun, maybe by a lot, it rotates about 65 times faster than the Sun, yet it produces about the same X-ray output. However, once the X-ray emission is scaled by L_{bol}, we find a logarithmic L_X/L_{bol} ratio of −7.4, much lower than that of the Sun.

Alderamin is quite similar to Altair; it is also of spectral type A7IV-V, rotates very fast and again its oblique shape could be measured interferometrically by van Belle et al. (2006). The latter authors deduce a rotation period of 12 hours and conclude that Alderamin is rotating at 82% of its break-up velocity. Hünsch et al. (1998) find a rather weak X-ray source in the ROSAT all-sky survey data at the position of Alderamin with an X-ray count rate almost identical to that of Altair once scaled by the squared distance ratio, thus the X-ray luminosities are very similar. With the bolometric luminosity derived by van Belle et al. (2006) we find a logarithmic L_X/L_{bol} ratio of −7.7. Due to the optical brightness of these two stars no reliable *Gaia* data is available; the $B - V$ colors of both stars are identical, we thus assume the same for the BP-RP colors and use a value of 0.26.

Our third comparison star is the Sun, for which we obviously do not have direct X-ray measurements with ROSAT, XMM-Newton, eROSITA etc.. Determining the total solar X-ray luminosity from solar data is somewhat cumbersome, and we refer to Judge et al. (2003) for a detailed discussion of this issue. For our purposes we assume a solar X-ray luminosity of 2×10^{27} erg/s, which ought to be a fair cycle average at soft X-ray wavelengths, however, as pointed out by Judge et al. (2003), the peak-to-peak cycle variations can be up to a factor of ten even outside flares. The equatorial rotation period of the Sun is is well known to be 25.67 d, and we assume a BP-RP color of 0.82. With this X-ray luminosity, we obtain an L_X/L_{bol} ratio of −6.3.

Finally, we consider a very nearby star, Barnard's star, which is of very late spectral type M4 with a BP-RP color of 2.83; González Hernández et al. (2024) provide a detailed discussion of the rotation period of Barnard's star and conclude that it is about 150 d. Previously, X-ray emission from Barnard's star had been reported by Schmitt et al. (1995) at a level of about 4×10^{25} erg/s, thus making it one of the weakest known X-ray sources outside of the solar system. With a bolometric luminosity of 3.5×10^{-3} $L_\odot$, we then finds a logarithmic L_X/L_{bol} ratio of −5.54, thus the star with the lowest X-ray luminosity and slowest rotation is the most active one when considered w.r.t. L_X/L_{bol}. It is very important to realize that the X-ray luminosities of our sample stars with successful period measurements are very much different from these selected low activity stars as demonstrated in Fig. 7, which re-emphasizes the point that a shallow all-survey as eROSITA misses out the bulk of the low-activity stellar population with X-ray properties like our Sun, this population can only be detected – if at all – in the immediate vicinity of the Sun and therefore contributes only very small numbers to the overall X-ray source population.

3.3. Period activity relations

We return to a discussion of Fig. 7, where we can very clearly notice the so-called onset of convection, a phenomenon that is well known in X-ray studies of late-type stars (Schmitt et al. 1985). Here, the number of sources with colors BP-RP > 0.6 and periods >1 d is rapidly increasing. However, we also notices two regions with somewhat "strange" rotation periods (i.e., in the color range ≈0.4 < BP-RP < ≈0.65 with rotation periods near 13 days) and another alias peak near 6 days. It is likely that the accumulation of stars near these periods is instrumental; therefore, we flag the sources inside the green dashed line in Fig. 7 to be able to identify these sources in our subsequent analyses; these sources are marked with the flag PB in Table B.1. Finally, we note that the paucity of stars with colors in excess of BP-RP ∼1.2 (as seen in Fig. 7) is a selection effect. This is because in a flux-limited X-ray survey, the sampled volumes for redder dwarf stars become smaller and smaller with increasing color, since the X-ray luminosities of the underlying stars are limited by the so-called saturation limit, which we discuss in detail in Sect. 3.7.

3.3.1. X-ray activity versus period

In this section, we study how the X-ray activity of our sample stars as measured through the fractional X-ray luminosity, L_X/L_{bol}, varies with the measured TESS periods. For comparison, we also add the stars already studied by Wright et al. (2011) using the same X-ray data and period measurements available at the time, yet with their V-K colors converted to BP-RP colors using the tables presented by Pecaut & Mamajek (2013). We consider stars of type F, G, K, and M separately, distinguish between early and late F-type stars and plot the measured L_X/L_{bol}-ratios versus period in Fig. 8.

Starting with the M-type stars displayed in the bottom panel of Fig. 8, we note that the short-period stars in this spectral range do reach a level of about $L_X/L_{bol} \sim 10^{-3}$, which is maintained for rotation periods of up to about seven days, and for longer periods, we see a clear drop in the activity levels; as also evidenced by Fig. 8, this spectral range is well populated by stars contained in the sample by Wright et al. (2011). Moving on to the K-type stars in our sample (displayed in the second panel

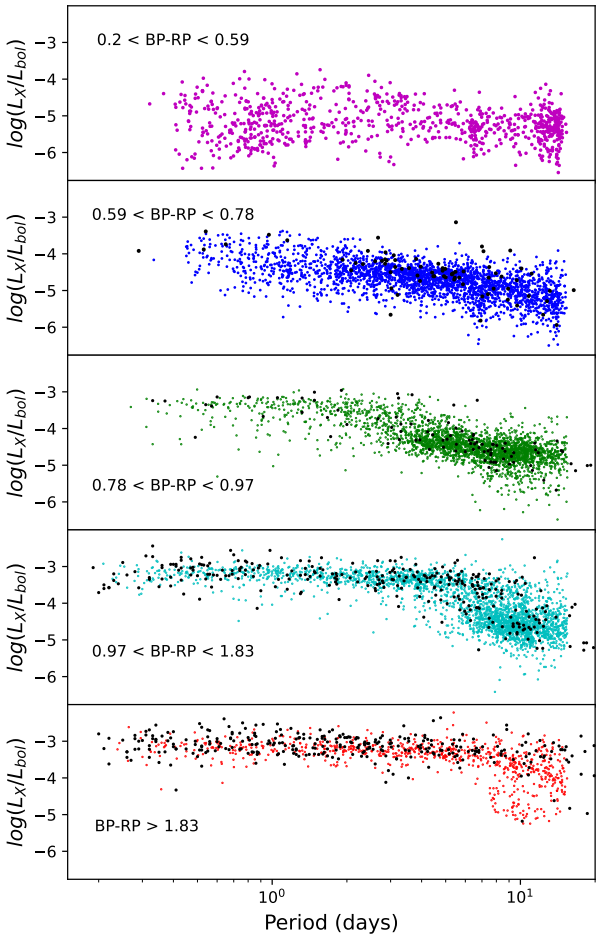

Fig. 8. log(L_X/ L_{bol}) vs. logarithmic period for MS stars in our sample; the stars studied by Wright et al. (2011) are indicated by black dots. See text for details. Top panel: stars in the color range 0.2 < BP-RP < 0.59, dubbed early F-type stars. Second panel from top: Stars in the color range 0.59 < BP-RP < 0.78, dubbed late F-type stars. Third panel from top: Stars in the color range 0.78 < BP-RP < 0.97, dubbed G-type stars. Second panel from bottom: Stars in the color range 0.97 < BP-RP < 1.83, dubbed K-type stars. Bottom panel from top: BP-RP > 0.78, M-type stars.

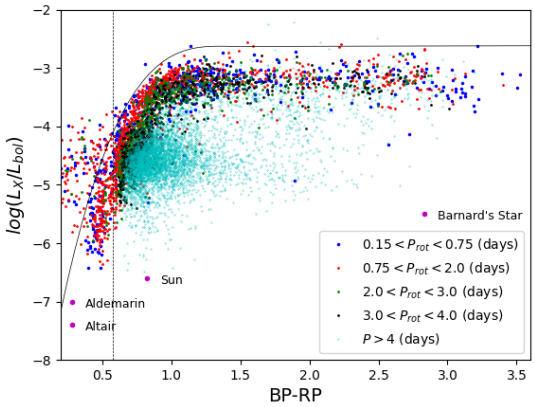

Fig. 9. L_X/ L_{bol} vs. BP-RP color for stars in various period ranges. The stars studied by Wright et al. (2011) are indicated by black dots. See text for details.

from the bottom in Fig. 8), we again find that the short-period stars in this spectral range do reach a level of about L_X/ L_{bol} ~ 10^{-3}, a bit lower than that reached by the M-type stars; this level is maintained for rotation periods of up to about four days and for longer periods, we see a clear drop in the activity levels. This spectral range is also well populated by stars contained in the sample by Wright et al. (2011). Considering next the G-type stars in the medium panel of Fig. 8, we clearly note that the saturation limit for G-stars does not reach the value of L_X/ L_{bol} ~10^{-3}; rather, it is found at a value of about L_X/ L_{bol} ~ 6 10^{-4} and a clear drop in L_X/ L_{bol} is very much apparent apparent for periods longer than about 3 days. Hence, we observe a very clear dependence of L_X/ L_{bol} on the period. The number of G-type stars in the short-period range reported by Wright et al. (2011) is rather small, yet the objects we are obviously missing in our eROSITA sample are truly low-activity stars, such as the Sun, with a period of 25 days or more and L_X/ L_{bol}-value of a few times 10^{-7} (cf., Fig. 9). Finally, we turn to the F-type stars plotted in the two upper panels of Fig. 8, where we subdivided our sample in early and late F-type stars using BP-RP = 0.59 as the break point between the two groups. First, it is clear that among the F-type stars, we found no star reaching the canonical saturation limit at L_X/ L_{bol} ~ 10^{-3}, the empirical saturation limit for those stars with BP-RP > 0.59 appears to lie closer to L_X/ L_{bol} ~ 10^{-4}; for the earlier F-types, it is near L_X/ L_{bol} ~ 10^{-5} (if we want to talk about saturation at all). We note that these two groups of stars show different period dependences in their L_X/ L_{bol}-ratios: the earlier types (top panel in Fig. 8) do not show any period dependence whatsoever, while the later types (second panel from top in Fig. 8) appear to be constant for periods below about 2 days, followed by clearly decreasing L_X/ L_{bol}-ratios, with increasing periods as seen for the stars of later spectral types.

3.3.2. X-ray activity versus color

For almost all spectral types of stars shown in Fig. 8, we notice a saturation level for the shorter periods, which, however, depends on spectral type. While for the later type K and M type stars this level lies a little bit below L_X/L_{bol} ≈ 10^{-3}, such values are definitely not reached by F-type stars. Furthermore, the activity-period dependence for stars below the saturation limit varies with spectral type: even though we see that for the earliest F-type stars, no period dependence is recognizable, the period dependence starts at around two days for the later types and that threshold moves up to around nine days for M-type stars. This finding is clearly not new, but was already realized in the studies by Pizzolato et al. (2003) and Wright et al. (2011), except that these studies contained only few G-stars and even fewer F-type stars (cf., Fig. 8).

With our new period measurements, we can now put the saturation limit in context and revisit the relation between X-ray activity and color, differentiated according to the stellar period. In Fig. 9, we consider our sample stars with secure periods and plot their activity as measured through their L_X/L_{bol} ratio as a function of BP-RP color with the different period ranges indicated by different colors as indicated in the legend of Fig. 9. For the purposes of orientation and discussion, we also added the four low-activity stars discussed in detail in Sect. 3.2 in Fig. 9.

Figure 9 shows a very rather sharp upper boundary of the measured L_X/L_{bol}-ratios already apparent in the eROSITA population studies by Freund et al. (2024), however, as apparent from Fig. 9, the most active stars in terms of L_X/L_{bol} at a given BP-RP color are those with the shortest periods, as expected. Furthermore, most of the "noise" apparent in Fig. 7 has disappeared, a few stars remain in the spectral range 0.2 < BP-RP < 0.6,

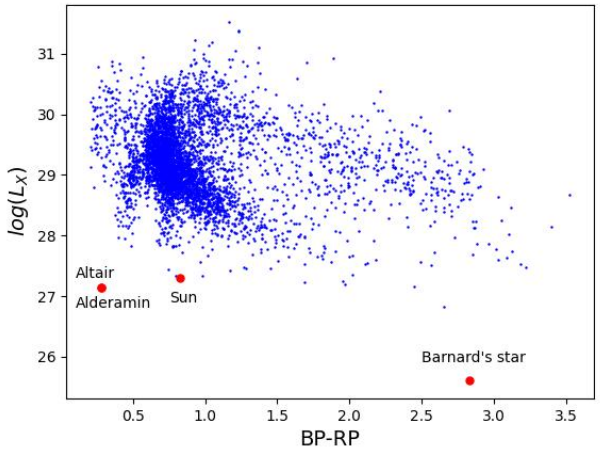

Fig. 10. X-ray luminosity L_X vs. BP-RP color for sample stars with successful period measurements as well as the selected low activity stars (red data points). See text for details.

which show no period dependence in their X-ray activity; population simulations (cf., Sect. 3.8) suggest that these objects could be binaries with the low mass companion responsible for the observed X-ray emission. In Fig. 10 we then examine the X-ray luminosities of our sample stars; we specifically note that the stars in the color range 0.2 < BP-RP < 0.6 do not appear to differ substantially from those of later spectral types, which suggests a binary interpretation: these stars ought to be rather young, thus, if accompanied by a late-type companion of type G or K, X-ray luminosities in the range of a few 10^{29} erg/s are not at all unusual; this would explain both the lack of any dependence on rotation and the measured L_X/L_{bol}-ratios.

Therefore, Fig. 9 demonstrates that activity of cool stars as measured through the L_X/L_{bol} ratio drops by two orders of magnitude over a rather narrow range of stellar color between 0.6 < BP-RP < 1.0 corresponding to a spectral type between about F6 and G9. This could arguably have to do with some "overcorrection" of the X-ray luminosities by the bolometric luminosities; however, the latter change only by a factor of six or so over the same spectral range, so this cannot be the correct explanation. Also, the rotation period alone cannot lead us to the correct explanation. While the Sun and (even more so) Barnard's star are located well below the observed L_X/L_{bol}-ratios encountered in the relevant color ranges, the extremely fast rotators Altair and Alderamin have the lowest activity values (in terms of L_X/L_{bol}) of all stars considered in seeming contradiction to any rotation-activity paradigm.

3.4. Convective turnover time and Rossby number

As made apparent in Sect. 3.3.2, we clearly have to look out for yet another stellar property to properly understand and interpret Fig. 9. However, we must also consider what stellar property changes by several orders of magnitude in the relevant spectral range. The natural answer obviously is the property of the stellar convection zones and their dramatic changes, with K stars having rather deep convection zones comprising significant fractions of stellar radius, while those of F-type stars become thinner and thinner. However, we must also consider how this relates to the question of activity saturation.

As shown by Noyes et al. (1984) for a sample of chromospherically active stars and by Pizzolato et al. (2003) and Wright et al. (2011) for a sample of X-ray active stars, we can "normalize" the rotation periods of stars of different spectral type by scaling the observed rotation periods with the so-called convective turnover time, which yields the Rossby number, and relate the activity properties to this Rossby number: by "forcing" the observed distributions of L_X/L_{bol} ratios and rotation periods, P_{rot}, to a common scale for all their sample stars, both Pizzolato et al. (2003) and Wright et al. (2011) were able to derive empirical convective turnover times (and eventually Rossby numbers) as a function of stellar color or stellar mass.

Motivated by the good agreement between the convective turnover times as calculated by Landin et al. (2023) and empirically derived ones by Wright et al. (2011), we decided to proceed with an empirical fit to the τ_{conv} BP-RP relation. Following Noyes et al. (1984), we chose a third-order polynomial for colors up to some value $(BP-RP)_{break}$, followed by a linear relation for redder colors. Abbreviating X = (BP-RP) - $(BP-RP)_{break}$, we can construct the ansatz,

$$\begin{aligned} log(\tau_{conv}(X)) &= T_0 + C \times X + B \times X^2 + A \times X^3 \quad \text{for} \quad X < 0, \\ &= T_0 + C \times X \qquad\qquad\qquad\quad \text{for} \quad X > 0, \end{aligned} \tag{3}$$

with four free parameters A, B, C, and T_0, which, together with the known BP-RP colors, determine τ_{conv} (specified in days). This analytical ansatz also requires the specification of a break point between the two color regimes; we choose BP-RP = 1.2, which agrees well with the computations by Landin et al. (2023) and is consistent with the choice of Noyes et al. (1984), who used B-V = 1.

Once the values of the convective turnover times are specified (e.g., those calculated from Eq. (3) using the measured BP-RP colors), we can compute a Rossby number using the also measured period for every sample star and thence – following the nomenclature by Wright et al. (2011) – produce a R_X (=L_X/L_{bol}) versus Rossby number (Ro) diagram. Both Pizzolato et al. (2003) and Wright et al. (2011) used a (logarithmic) broken power-law description, namely, based on relationships between R_X and Ro taking the form of

$$\begin{aligned} R_X(Ro) &= R_{X,sat} \qquad\qquad\qquad\quad \text{for} \quad Ro < Ro_{break}, \\ &= R_{X,sat} \times \left(\frac{Ro_{break}}{Ro}\right)^{\beta} \quad \text{for} \quad Ro > Ro_{break}, \end{aligned} \tag{4}$$

with the slope, β, the saturated Rossby number, $R_{X,sat}$, and the Rossby number break point, Ro_{break}, at the break point between the two dependences. This allowed them to devise a simple model, referred to as model A in the following, with only three independent parameters. Using this approach, Pizzolato et al. (2003) and Wright et al. (2011) were able to obtain good empirical descriptions of the activity properties of their respective stellar samples. Naturally, Eq. (4) is quite arbitrary and it might be preferable to adopt other forms without a break. One such possibility is given by the ansatz,

$$R_X(Ro) = A_0 \times e^{-Ro/\lambda} + A_\infty \times \frac{e^{-\lambda/Ro}}{Ro^{\beta}}, \tag{5}$$

with the free parameters A_0, A_∞, λ, and β, referred to as model B in the following. In Eq. (5), we obviously have $\lim_{Ro\to 0} R_X(Ro) = A_0$, where A_0 is the saturation limit and asymptotically for $\lim_{Ro\to\infty} R_X(Ro)$, we have $R_X \sim A_\infty\ Ro^{-\beta}$ (i.e., the β parameters in Eqs. (4) and (5) are the same). Obviously, Eq. (5) is as arbitrary as Eq. (4) in the sense that is a purely empirical ansatz without any theoretical foundation, yet it yields a differentiable function. We note that in Eq. (5), the saturation level is reached only asymptotically.

3.5. X-ray activity versus Rossby number

To study the relationship between X-ray activity (as measured through the L_X/L_{bol} ratio) and Rossby number, we used Eqs. (4) and (5) as empirical descriptions for the computation of the expected activity (in terms of L_X/L_{bol}). However, instead of using binned versions of convective turnover time as Wright et al. (2011), we use the analytical description of convective turnover time given by Eq. (3). Our model thus consists of the three parameters, β, the saturated, $R_{X,sat}$, and the Rossby number, Ro_{break}, for the model defined by Eq. (4) and the four parameters A_0, A_∞, λ, and β for the model defined by Eq. (5), describing the X-ray activity-Rossby number relationship and of the four parameters A, B, C, and T_0, describing the dependence of convective turnover time on BP-RP color. Thus, the overall models have seven or eight free parameters, respectively. However, to reduce the number of free parameters we fix the value of β at 2 (as in Wright et al. 2011) and, next, we chose the parameter Ro_{break} (in Eq. (4)) and A_∞ (in Eq. (5)). Furthermore, as discussed in Sect. 3.4 the break point between the two regimes in the τ_{conv}-BP-RP relation is fixed at BP-RP = 1.2, which results in convective turnover times for the Sun that agree with the usual expectations.

Given set of values for the parameters A, B, C, and T_0, we can compute the values of convective turnover time for each sample data point. Combined with the measured period, this allows for an estimate of the Rossby number, *Ro*, for every sample star star and, hence, an estimate of this star's R_X-value using Eqs. (4) or (5), which can be compared to the observed R_X ratios. While this appears to be a straightforward non-linear fitting problem with seven or eight parameters, we ran into a number of difficulties in arriving at stable solutions. The main problem here are interlopers (i.e., obviously wrong data data points). Such interlopers could be caused by erroneous identifications of the X-ray sources, by incorrect period determinations, by errors in the assumed stellar parameters, and (perhaps most importantly) through the presence of unrecognized binaries. An illustrative example for the latter case is the well known nearby star α CrB, consisting of an A0V primary and a G2V secondary component. Fortuitously, this system is eclipsing and during optical secondary eclipse (i.e., A star in front of G star) the system's X-ray flux drops to zero as shown by Schmitt & Kürster (1993), demonstrating that the X-ray emission exclusively comes from the later type star. If this system were not known to be a binary system, our scheme would attribute the X-ray emission to a relative fast rotating A-type star, which would be clearly wrong, and such wrong data points can severely "contaminate" any straightforward "best-fit" solution.

To deal with such an interloper population we analyzed our data using a so-called "mixture model", namely, the data were modeled by two populations, one genuine population obeying Eqs. (4) or (5) and an interloper population modeled by a noise distribution. Every data point was assigned a probability, q, of being part of the genuine population and $1 - q$ to be part of the interloper population. For a detailed explanation and discussion of this approach, we refer to the illuminating blog by Foreman-Mackey (2014), who also provides *Python* code examples.

We set up a mixture model composed of two populations: one genuine population described by the seven or eight parameters, A, B, C, T_0, and β, $R_{X,sat}$ and Ro $_{break}$ or A_0, A_∞, λ, and β, along with some fraction, q; and an interloper population, following Foreman-Mackey (2014) described by a Gaussian distribution with some mean and dispersion, contributing a fraction of $1 - q$ to the overall population. To solve this problem, we used the emcee code developed by Foreman-Mackey et al. (2013), which utilizes an affine-invariant ensemble sampler for a Markov chain Monte Carlo (MCMC) computation, as introduced by Goodman & Weare (2010). We iterated the emcee produced MCMC chains until convergence, which we considered to be achieved when the total likelihood no longer showed any trends and, thus, the MCMC burn-in phase was achieved. From this state, we start the production run for which we use 64 walkers and 1000 iterations. For both the initial burn-in and subsequent production, we would need to put priors on some parameters. As in Wright et al. (2011), we needs to constrain the slope of the rotation-activity relation (i.e., setting the β parameter in model A to 2) to arrive at stable solutions. In model B, we fixed the β parameter again at 2 and the A_0 parameter at 3. The priors for the remaining parameters were chosen as flat priors with generous ranges around the "expected" values; care must be applied to the prior for the saturation limit and the λ parameter (in case of model B) to ensure that the MCMC chain converges at a reasonable solution.

Table 2. Fit results convective turnover time and Rossby number.

	ER. (3) + Eq. (4)		Eq. (3) + Eq. (5)
A	5.11 ± 0.15	A	4.74 ± 0.154
B	1.18 ± 0.10	B	1.15 ± 0.10
C	0.506 ± 0.006	C	0.42 ± 0.01
T_0	18.30 ± 0.005	T_0	16.722 ± 0.005
$\log(R_{X,sat})$	−3.313 ± 0.008	A_0	−3.0 (fixed)
		λ	$6 \times 10^{-2} \pm 8 \times 10^{-5}$
β	2.0 (fixed)	β	2.0 (fixed)

From the production run chains, we computed the mean values and dispersion of all fit parameters and in particular for the parameters A, B, C, and T_0, which define the convective turnover times. Following the approach described by Foreman-Mackey (2014), we then computed membership probabilities for each individual sample star. In Table 2 and in Figs. 11 and 12, we show the results of these computations. In Table 2, we present the derived fit parameters for the two cases considered. Each of the figures contains two panels, showing L_X/l_{bol} versus Ro with the top panels referring to the prescription Eqs. (3) and (4), while the bottom panels use the prescription Eqs. (3) and (5). In Fig. 11 we concentrate on the individual data points, while in Fig. 12 we concentrate on the sample properties with respect to spectral type. In Fig. 11 the membership probabilities, p_{mem}, of our sample stars are color-coded; green data points indicate stars with $p_{mem} > 0.5$, blue data points stars with $0.3 < p_{mem} < 0.5$, and red data points indicate stars with $p_{mem} < 0.3$. Also shown in Fig. 9 are the four stars Altair, Alderamin, the Sun, and Barnard's star discussed in detail in Sect. 3.2; while Barnard's star lies in the range of sampled L_X/L_{bol} ratios, the Sun and in particular Altair and Alderamin lie several orders of magnitude below the sampled activity range, but within the reach of the X-ray activity versus Rossby number relation defined by Eqs. (4) or (5), even if the scatter around the median is quite substantial.

The many partially overlapping data points in Fig. 11 obstruct our view of the sample properties. Therefore, in Fig. 12 we concentrate on the sample properties differentiated by spectral type. The overall density of our data points is indicated by the gray shaded area, the medians of the distributions are given by the blue (A-type stars), green (F-type stars), yellow (G-type stars), magenta (K-type stars) and red (M-type stars) thick lines, the contours are also shown. The expected mean relations between

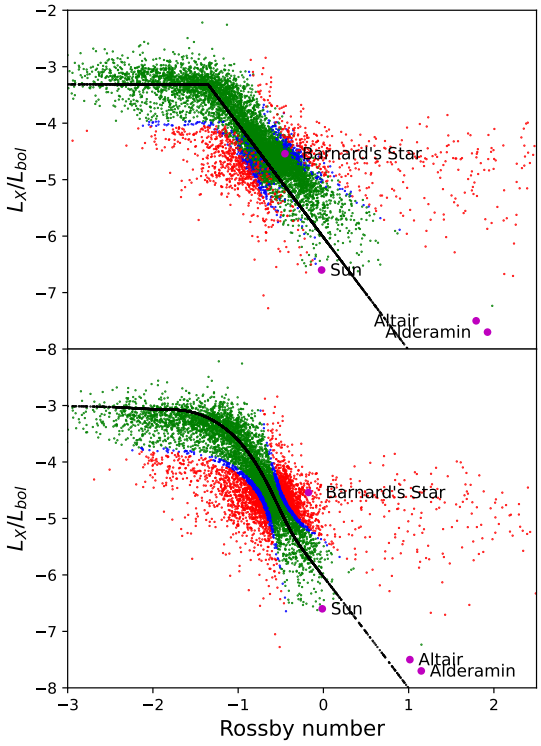

Fig. 11. L_X/L_{bol} ratio vs. Rossby number for our sample stars with the different colors indicating different membership probabilities (green largest, red lowest), the black line is the best fit with the functional form as given by Eqs. (4) (top panel) and (5) (bottom panel). See text for details.

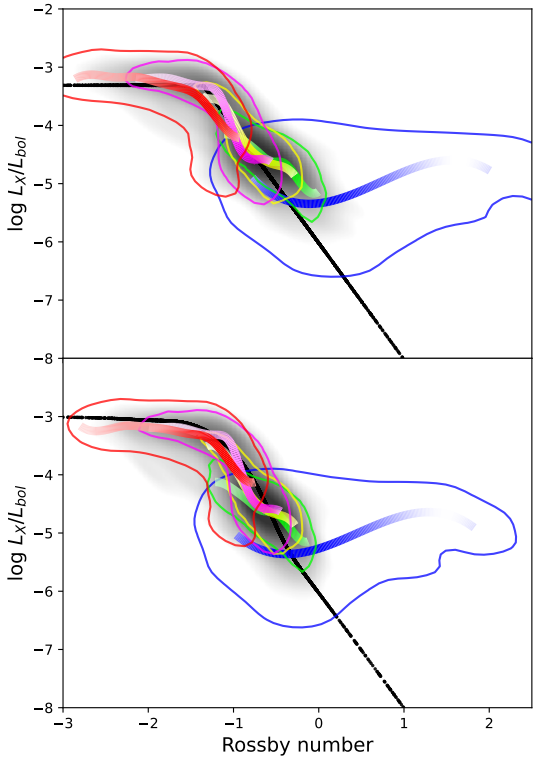

Fig. 12. L_X/L_{bol} ratio vs. Rossby number for our sample stars with the different colors indicating the different spectral types: blue indicating A and early F-type stars, green late F-type stars, yellow G-type stars, magenta K-type stars, and red M-type stars. Population medians (thick line) and the 90% contours (thin lines) of the population are also shown. The gray-shaded area indicates the density of the data points, the black line is the best fit with the functional form as given by Eqs. (4) (top panel) and (5) (bottom panel). See text for details.

the L_X/L_{bol} ratio and Rossby number are provided by the black colored line, calculated with the parameters specified in Table 2. A comparison of Figs. 11 and 12 shows that the forbidden red data points in Fig. 11 exclusively correspond to A-type stars and therefore very likely do not indicate emission from these objects in contrast to the cases of Altair and Aldemarin shown in Fig. 11. The medians of the other stellar types agree rather well although there might be differences in particular for the F-type stars; as noted earlier, the F-type and G-type stars do not reach the saturation level of $\approx 10^{-3}$ in L_X/L_{bol} and never reach Rossby numbers of 0.01.

Some support for this scenario can be derived from *Gaia* data. We specifically investigated 160 large Rossby number sources shown in Fig. 11, i.e., source with formal Rossby numbers in excess of 10. Out of these 16 (i.e., 10%) were found to have the non-single-star flag set in the *Gaia* catalog implying that the binary fraction in this subsample appears to be much larger than in the *Gaia* catalog at large. However, a systematic investigation of this issue would go far beyond the scope of this paper.

3.6. Convective turnover time

As a byproduct of our fitting exercise, we also obtained the parameters A, B, C, and T_0, which define our estimate of the convective turnover time as a function of BP-RP color. The results for the nominal fit parameters are shown in Fig. 13; from the MCMC chains, we estimated the parameters A, B, C, T_0, and their dispersion, which define the estimates for the convective turnover times for the case of Eqs. (4) (blue curve) and (5) (red curve). For comparison, we also show the results of the model

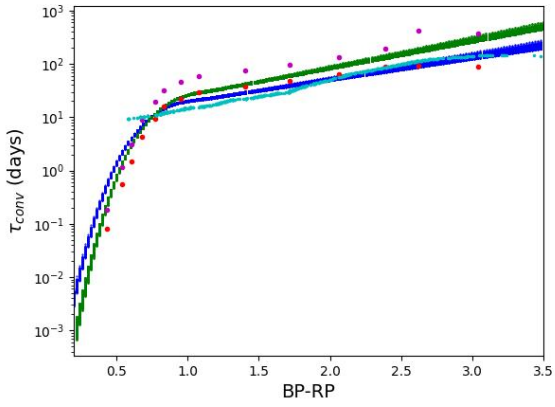

Fig. 13. "Best-fit" convective turnover time vs. BP-RP colors (derived from Eq. (4) as blue solid curve, derived from Eq. (5) as green solid curve); the shown data points (global convective turnover time in red, local convective turnover time in magenta) come from the theoretical calculations by Landin et al. (2023), the cyan data points are derived from the sample presented by Wright et al. (2011). See text for details.

calculations by Landin et al. (2023) as well as the data points provided by Wright et al. (2011). Our best-fit curves follow the values for global and local turnover time for most of the parameter range rather closely; however, for smaller BP-RP colors, we obtained slightly larger values. Also, we remark that this value only sets the scale for the Rossby number. We further note

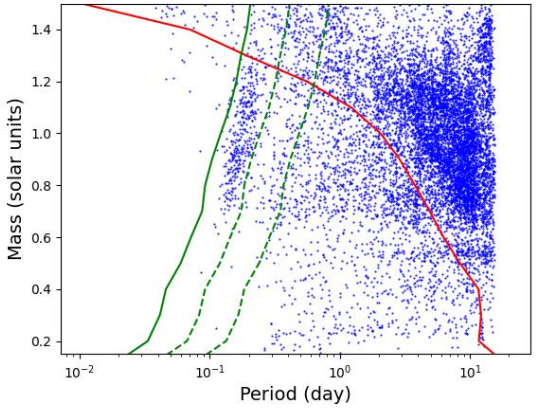

Fig. 14. Mass (in solar units) vs. period (in days) for our MS sample, with masses estimated from the stars' BP-RP colors using data tables from Pecaut & Mamajek (2013). The red solid line is the period computed from Eq. (4) at the Rossby break point, Ro_{break}, and the convective turnover time computed from Eq. (3). The green lines show the break up periods computed from Eq. (1). See text for details.

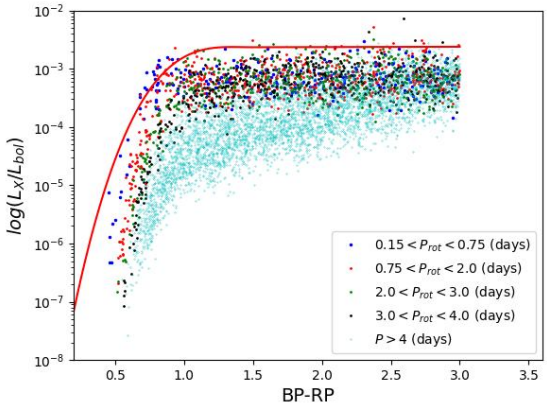

Fig. 15. Toy model simulation of the L_X/L_{bol} ratio vs. BP-RP color for the eROSITA detected cool star population. See text for details.

that the values computed by Wright et al. (2011) reproduce the trend for colors BP-RP > 0.9, but obviously the range of F-type stars and early G-type stars is not really covered by the sample of Wright et al. (2011) and the massive decrease in convective turnover time in this spectral range is missed altogether.

3.7. The saturation limit and cool stars

Clearly, this leads us to wonder whether the agreement between theory and observations is coincidental or physical. However, if the relations given by Eqs. (4) or (5) and the run of convective turnover time with mass (and, hence, BP-RP color) hold over the whole parameter range of cool stars, then it is clear that stars with increasing mass (and, thus, decreasing convective turnover time) find it exceedingly difficult to reach the small Rossby number regime and, hence, the saturation limit, since they would have to rotate with periods substantially below their convective turnover time, which are becoming quite small already. Using the expression in Eq. (3) and our fit results, we can address the question of which period range is available to stars with respect to a rotation that is, on the one hand, slow enough to stay above their respective break-up period, but rotate, on the other hand, rapidly enough to enter the saturation regime. The results are shown in Fig. 14, where we plot the measured periods and estimated masses for our sample stars. Also shown is the convective turnover time (red line, as computed from Eq. (3)) as well as the estimated break-up periods for 100, 50, and 10% of the estimated break-up level (green lines). To enter the saturation regime without breaking up, a star must lie below the red and green curves. As is obvious from Fig. 14, there is only a restricted range of periods available for saturation and stars with masses above $\approx$1.2 $M_\odot$ simply cannot rotate rapidly enough to ever enter the saturation regime.

The problem of X-ray saturation has been around for a while and Wright et al. (2011) presented a detailed account of this issue. Wright et al. (2011) specifically stated that in their sample "a mean saturation level of $\log(R_X) = -3.13 \pm 0.22$, almost independent of spectral type" was found, yet they also stated that "a significantly lower mean saturation level for the highest-mass stars in their sample (F-type stars)" was found as well. However, Wright et al. (2011) then argued that these stars (i.e., F-type stars) are not saturated but "super-saturated" and that therefore the saturation level is independent of spectral type. We note that super-saturation refers to the phenomenon that for very fast rotators, the fractional X-ray luminosity, R_X, appears to decrease, yet the evidence for the phenomenon is scarce as stated by Wright et al. (2011). Furthermore, these authors discuss in particular the so-called "polar updraft" effect introduced by Stępień et al. (2001) in a study of W UMa-systems and the so-called "centrifugal stripping" effect, introduced by James et al. (2000) in a study of M dwarfs. In the case of a rotating star, the von Zeipel theorem states that the emergent radiative flux is proportional to the local gravity, which becomes smaller and smaller with increasing rotation rate, and as a consequence the flows and hence convective motions in the polar direction differ substantially from those in equatorial direction. In the "coronal stripping" scenario developed by James et al. (2000), the location of the co-rotation radius with respect to the stellar radius is a primary focus. Inspecting the relevant formulae for both scenarios, we realize right away that the critical point is reached if a star were to rotate with its break-up period given by Eq. (1); in this case, the equatorial effective gravity would vanish and the co-rotation radius would coincide with the stellar radius.

For the more massive stars, these scenarios yield almost identical results, since the radius of the radiative-convective boundary moves close to the stellar radius and at the equator the two expressions (Eqs. (6) and (8) in Wright et al. 2011) become identical. Furthermore, $R_{Kepler}/R_* = 1$ and $G_X = -1$ (in the notation of Wright et al. 2011) represent the absolute limit if we postulate that stars cannot rotate beyond break-up, with the consequence that most of the region dubbed "supersaturated" in Fig. 5 of Wright et al. (2011) cannot be populated at all. Evaluating then the break-up period of a star with a mass of 1.5 $M_\odot$ and radius 1.64 $R_\odot$ we find a break-up period of 0.19 d, yet the models by Landin et al. (2023) yield a convective turnover time below 0.01 d, implying that these stars can never reach the break-point in Rossby number beyond which saturation takes place. In other words, these stars can never become saturated, not to mention supersaturated.

3.8. The cool star eROSITA population at large

With the results obtained above, it is now possible to understand the color and X-ray activity distribution of the cool star population in an X-ray survey such as eROSITA. While a detailed population simulation and study would go far beyond the scope of the present paper, we wish to demonstrate this possibility with a "toy model", that encompasses all the relevant

features but is not meant to model the specific eROSITA population of cool star X-ray sources. For this purpose we perform a Monte Carlo simulation of a population of MS cool stars with uniformly distributed distances from the Sun in a spherical volume out to 100 pc and BP-RP colors again uniformly distributed; furthermore we assume that the statistical distribution of rotation periods is known which we again assume to be uniform. Since the BP-RP color determines (more or less) stellar mass, radius and bolometric luminosity, we can then compute the break-up period from Eq. (1) , the convective turnover time from Eq. (3), and the L_X/L_{bol} ratio from Eqs. (4) or (5) for the whole population. Since L_{bol} and the distance of each source are known, the X-ray luminosity, L_X, and the apparent X-ray flux f_X for every source can be computed. For simplicity, we assumed a uniform survey flux limit of 1×10^{-14} erg/cm^2/s for the whole survey; hence, we were able to assess whether the considered source is detected in the survey or not. We performed this simple Monte Carlo simulation with 10 000 trials and reject any source with a period below the break-up period. In this fashion, we were able to construct a simulated L_X/L_{bol} versus Rossby number diagram displayed in Fig. 15. In Fig. 15, we distinguish between stars with different rotation periods using the same period bins as in Fig. 9. Furthermore, the red solid curve shown in Fig. 15 is identical to the upper envelope to the observed distribution shown in Fig. 9, indicating that it has not been derived from the simulated data. Thus, as is clear from Fig. 15, our rather simplistic toy model already reproduces the essential features of the eROSITA observed cool star population, suggesting that the relevant physics has been incorporated in the model.

4. Conclusions

Using TESS short-cadence photometry of eROSITA detected cool stars, we determined periods for more than 14 000 objects with consistently measured X-ray fluxes. As a result, we have created the largest available sample to date of cool stars with measured X-ray luminosities and rotation periods. Several comparisons with independently determined periods show that the percentage of incorrectly determined periods must be low, despite the rather massive contamination of TESS data by instrumental effects in some instances. We show that a key element for the interpretation of the X-ray data is the convective turnover time required to compute Rossby numbers. Our determinations of convective turnover times extend over the full range of late-type stars and yield results that are very much consistent with theoretical model calculations; however, they extend only to early F-type stars. To compute Rossby numbers, we used the classical broken power-law description between fractional X-ray luminosity, L_X/L_{bol}, and the Rossby number, but we also introduced a smooth parametrization of the period-activity relations observed at X-ray wavelengths. Our new data confirm previously determined relations between activity as measured though the L_X/L_{bol} ratio and Rossby number, while for the "earlier" late-type stars (specifically of types F and early G), the stellar sample presented in this paper enables a detailed investigation of the period-activity relationships in these stars for the first time at X-ray wavelengths. Both our empirical modeling as well as theory suggest very low turnover times, mainly due to the small sizes of convection zones in these stars. This result implies that extremely rapid rotators can never reach the saturation level as observed in stars of type K and M and, therefore, they remain "low-activity" stars despite their extremely rapid rotation. Finally, we demonstrate that a rather simple toy model can explain the observed activity distribution (measured through L_X/L_{bol}) with respect to color (measured through *Gaia* BP-RP color) for the eROSITA-detected cool star X-ray population. We argue that the observed drop of activity by three orders of magnitude over a narrow color range between 0.6 < BP-RP < 1.0 results from the properties of the convective turnover times in these stars.

Data availability

The full Table 1 is available at the CDS via https://cdsarc.cds.unistra.fr/viz-bin/cat/J/A+A/709/A180

Acknowledgements. We thank our referee for the careful scrutiny of our paper and the many suggestions which let us considerably improve our paper. This work is based on data from eROSITA, the primary instrument aboard SRG, a joint Russian-German science mission supported by the Russian Space Agency (Roskosmos), in the interests of the Russian Academy of Sciences represented by its Space Research Institute (IKI), and the Deutsches Zentrum für Luft- und Raumfahrt (DLR). The SRG spacecraft was built by Lavochkin Association (NPOL) and its subcontractors, and is operated by NPOL with support from IKI and the Max Planck Institute for Extraterrestrial Physics (MPE). The development and construction of the eROSITA X-ray instrument was led by MPE, with contributions from the Dr. Karl Remeis Observatory Bamberg & ECAP (FAU Erlangen-Nürnberg), the University of Hamburg Observatory, the Leibniz Institute for Astrophysics Potsdam (AIP), and the Institute for Astronomy and Astrophysics of the University of Tübingen, with the support of DLR and the Max Planck Society. The Argelander Institute for Astronomy of the University of Bonn and the Ludwig Maximilians Universität Munich also participated in the science preparation for eROSITA. The eROSITA data used for this paper were processed using the eSASS/NRTA software system developed by the German eROSITA consortium. This work has made use of data from the European Space Agency (ESA) mission *Gaia* (https://www.cosmos.esa.int/gaia), processed by the *Gaia* Data Processing and Analysis Consortium (DPAC, https://www.cosmos.esa.int/web/gaia/dpac/consortium). Funding for the DPAC has been provided by national institutions, in particular the institutions participating in the *Gaia* Multilateral Agreement. This research has also made use of the SIMBAD database, operated at CDS, Strasbourg, France. This paper includes data collected with the TESS mission, obtained from the MAST data archive at the Space Telescope Science Institute (STScI). Funding for the TESS mission is provided by the NASA Explorer Program. STScI is operated by the Association of Universities for Research in Astronomy, Inc., under NASA contract NAS 5?26555.

References

Basri, G. 2021, An Introduction to Stellar Magnetic Activity (Oxford: IOP Publishing)
Basri, G., & Shah, R. 2020, ApJ, 901, 14
Borucki, W. J., Koch, D., Basri, G., et al. 2010, Science, 327, 977
Distefano, E., Lanzafame, A. C., Brugaletta, E., et al. 2023, A&A, 674, A20
Ferraz-Mello, S. 1981, AJ, 86, 619
Foreman-Mackey, D. 2014, Mixture Models, https://doi.org/10.5281/zenodo.15856
Foreman-Mackey, D., Hogg, D. W., Lang, D., & Goodman, J. 2013, PASP, 125, 306
Freund, S., Czesla, S., Predehl, P., et al. 2024, A&A, 684, A121
Gaia Collaboration (Arenou, F., et al.) 2023, A&A, 674, A34
González Hernández, J. I., Suárez Mascareño, A., Silva, A. M., et al. 2024, A&A, 690, A79
Goodman, J., & Weare, J. 2010, Commun. Appl. Math. Comput. Sci., 5, 65
Hedges, C., Hughes, A., Zhou, G., et al. 2021, AJ, 162, 54
Høg, E., Fabricius, C., Makarov, V. V., et al. 2000, A&A, 355, L27
Holcomb, R. J., Robertson, P., Hartigan, P., Oelkers, R. J., & Robinson, C. 2022, ApJ, 936, 138
Hünsch, M., Schmitt, J. H. M. M., & Voges, W. 1998, A&AS, 132, 155
Ioannidis, P., & Schmitt, J. H. M. M. 2020, A&A, 644, A26
James, D. J., Jardine, M. M., Jeffries, R. D., et al. 2000, MNRAS, 318, 1217
Jenkins, J. M., Twicken, J. D., McCauliff, S., et al. 2016, SPIE Conf. Ser., 9913, 99133E
Judge, P. G., Solomon, S. C., & Ayres, T. R. 2003, ApJ, 593, 534
Justesen, A. B., & Albrecht, S. 2021, ApJ, 912, 123
Lachaume, R., Dominik, C., Lanz, T., & Habing, H. J. 1999, A&A, 348, 897
Landin, N. R., Mendes, L. T. S., & Vaz, L. P. R. 2010, A&A, 510, A46

Landin, N. R., Mendes, L. T. S., Vaz, L. P. R., & Alencar, S. H. P. 2023, MNRAS, 519, 5304
McQuillan, A., Mazeh, T., & Aigrain, S. 2014, ApJS, 211, 24
Merloni, A., Lamer, G., Liu, T., et al. 2024, A&A, 682, A34
Mowlavi, N., Holl, B., Lecoeur-Taïbi, I., et al. 2023, A&A, 674, A16
Noyes, R. W., Hartmann, L. W., Baliunas, S. L., Duncan, D. K., & Vaughan, A. H. 1984, ApJ, 279, 763
Paegert, M., Stassun, K. G., Collins, K. A., et al. 2022, VizieR Online Data Catalog: TESS Input Catalog version 8.2 (TIC v8.2) (Paegert+, 2021), VizieR On-line Data Catalog: IV/39
Pallavicini, R., Golub, L., Rosner, R., et al. 1981, ApJ, 248, 279
Pecaut, M. J., & Mamajek, E. E. 2013, ApJS, 208, 9
Pizzolato, N., Maggio, A., Micela, G., Sciortino, S., & Ventura, P. 2003, A&A, 397, 147
Prša, A., Kochoska, A., Conroy, K. E., et al. 2022, ApJS, 258, 16
Ricker, G. R., Winn, J. N., Vanderspek, R., et al. 2015, J. Astron. Teles. Instrum. Syst., 1, 014003
Rieutord, M., Reese, D. R., Mombarg, J. S. G., & Charpinet, S. 2024, A&A, 687, A259
Robrade, J., & Schmitt, J. H. M. M. 2009, A&A, 497, 511
Santos, Â. R. G., Godoy-Rivera, D., Finley, A. J., et al. 2024, Front. Astron. Space Sci., 11, 1356379
Schmitt, J. H. M. M., & Kürster, M. 1993, Science, 262, 215
Schmitt, J. H. M. M., Golub, L., Harnden, Jr., F. R., et al. 1985, ApJ, 290, 307
Schmitt, J. H. M. M., Fleming, T. A., & Giampapa, M. S. 1995, ApJ, 450, 392
Schmitt, J. H. M. M., Ioannidis, P., Robrade, J., et al. 2021, A&A, 652, A135
Schmitt, J. H. M. M., Czesla, S., Freund, S., Robrade, J., & Schneider, P. C. 2022, A&A, 661, A40
Stępień, K., Schmitt, J. H. M. M., & Voges, W. 2001, A&A, 370, 157
Stellingwerf, R. F. 1978, ApJ, 224, 953
van Belle, G. T., Ciardi, D. R., Thompson, R. R., Akeson, R. L., & Lada, E. A. 2001, ApJ, 559, 1155
van Belle, G. T., Ciardi, D. R., ten Brummelaar, T., et al. 2006, ApJ, 637, 494
van der Woerd, H., Tagliaferri, G., Thomas, H. C., & Beuermann, K. 1989, A&A, 220, 221
Wright, N. J., Drake, J. J., Mamajek, E. E., & Henry, G. W. 2011, ApJ, 743, 48
Zechmeister, M., & Kürster, M. 2009, A&A, 496, 577

Appendix A: Three specific light curve examples: AV Dor, AB Dor, BD-11 1208

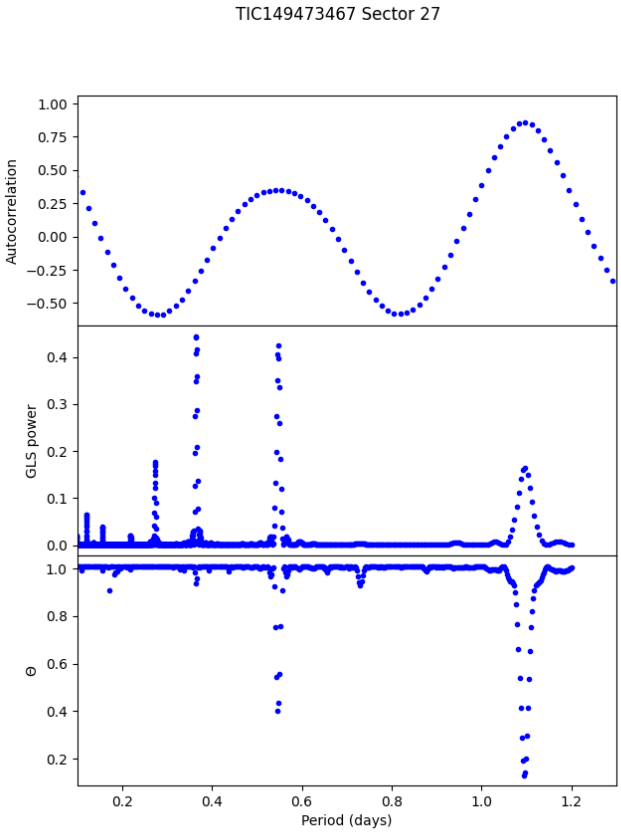

Fig. A.1: Period analysis for TESS data in sector 27 for AV Dor: Top panel: Autocorrelation vs. period. Medium panel: GLS power vs. period. Bottom panel: Θ vs. period.

In Appendix A we study how our period determination scheme works on well-known stars with known period properties to explore the limits of what can be done. We therefore consider some specific exemplary source types that give rise to strong periodic signals, namely, the eclipsing binary AV Dor, the ultra-active star AB Dor with strong spot-induced modulations, and the multi-period star BD-11 1208. The nature of these sources is well known and these examples were chosen to demonstrate the difficulties encountered in period determinations in general and especially in active stars; note that eclipsing binaries are usually also active when one or or both system components are of late spectral type.

A.1. AV Dor: An eclipsing binary

AV Dor (= TIC 149473467, spectral type F0) is a close binary with a period of 1.09 days, the TESS data of which have been analyzed by Justesen & Albrecht (2021). Because of its southern location AV Dor is frequently observed by TESS, and here we consider the TESS data obtained in sector 27. In Fig. A.1 we show the results of our period analysis of these data: in the top panel we show the measured autocorrelation function, in the medium panel the GLS periodogram and in the bottom panel the Θ-statistics in the phase dispersion minimization (for details see Stellingwerf 1978) in the period range 0.1 - 1.3 days. As apparent from Fig. A.1, the autocorrelation function shows two peaks at 0.545 days and at 1.09 days, the Θ statistics has two minima at the same periods. The GLS power spectrum shows several maxima, yet the maximum with the largest power has a negative autocorrelation, and the period with the largest autocorrelation and smallest Θ value has only the fourth largest power. The period 1.09 days is the correct period as evidenced by the folded TESS light curve of AV Dor displayed in Fig. A.2, which shows two eclipses (at phases of about 0.45 and 0.9) as well a photometric "wave", due to activity phenomena on both stars and the maxima of which are separated by a phase difference of 0.4.

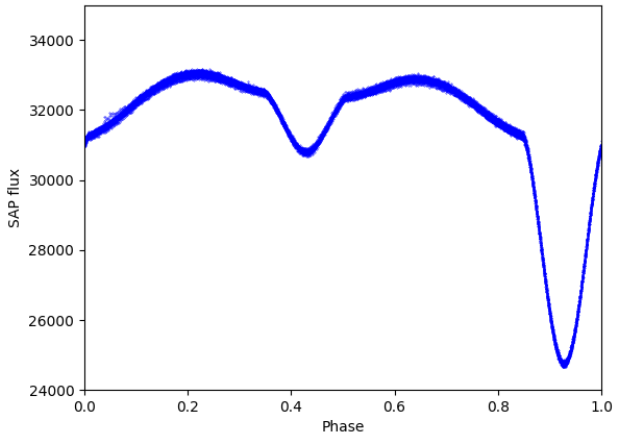

Fig. A.2: TESS light curve from sector 27 for AV Dor folded with the binary period of 1.09 days; see text for details.

A.2. AB Dor: An ultrafast rotator

We now consider the prototypical nearby ultra-active star AB Dor, which is also extensively observed by TESS due to its favorable southern location near the southern ecliptic pole; eROSITA and TESS data of AB Dor have already been presented by Schmitt et al. (2021). The rotation period of AB Dor is well known, with P_{rot} = 0.51428 days (Ioannidis & Schmitt 2020) it executes more than 50 rotations in a typical TESS sector and may exhibit photometric modulations of more than 10%, leading to an extremely "sharp" signal in Fourier space; a very detailed study of TESS data of AB Dor has been presented by Ioannidis & Schmitt (2020).

In Fig. A.3 we plot (analogously to Fig. A.1) the GLS periodogram (medium panel) for the TESS data on AB Dor in sector 27; the top panel shows the autocorrelation of the data, the bottom panel the Θ-statistics for the phase dispersion minimization. The GLS periodogram in Fig. A.3 does show the expected sharp Fourier peaks: one at the known rotation period of P_{rot} = 0.51428 days and the other peak appears at half this period as an alias, yet with even more Fourier power than the correct period peak. In the autocorrelation of the phased data (shown in the top panel of Fig. A.3), we can also recognize two much broader peaks at the same periods as in the periodogram, however, the phased light curve autocorrelation at the correct period is larger than that of the aliased period. Similar consideration apply to the Θ-statistics for the phase dispersion minimization; the Θ-statistics is smallest for the correct period, but there are aliases at half the correct period as well as integer multiple of these periods.

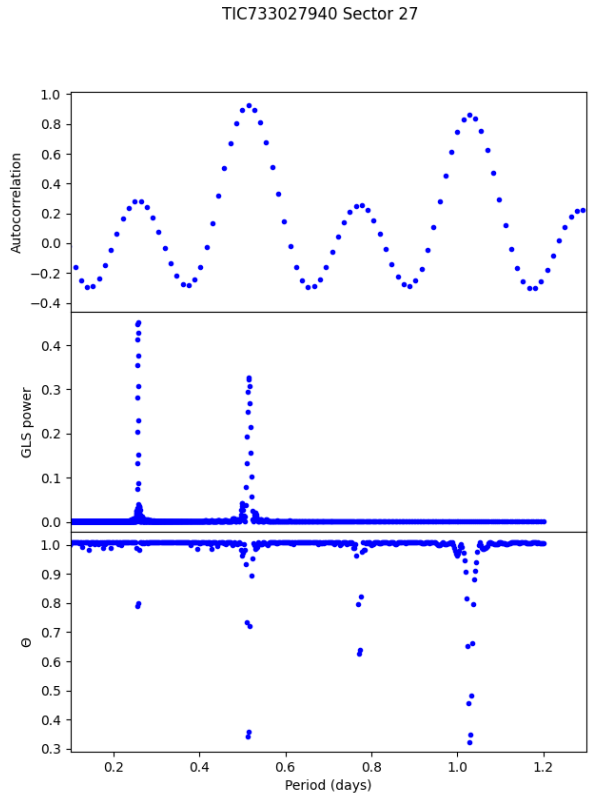

Fig. A.3: Period analysis for ultrafast rotator AB Dor with TESS sector 27 data. Top panel: Autocorrelation function vs. period. Medium panel: GLS power vs. period. Bottom panel: Θ vs. period.

It is instructive to examine the TESS data folded with the rotation period as plotted in Fig. A.4. We would immediately notice the substantial photometric variability of AB Dor even outside obvious flares, and the relative peak-to-peak amplitude is almost 14%. Furthermore, we can make note of the two flux minima, namely, phases when the surface spot concentration is largest: one, at about $\phi \approx 0.25$, and another one at $\phi \approx 0.8$ (i.e., almost exactly on the other side of the star).

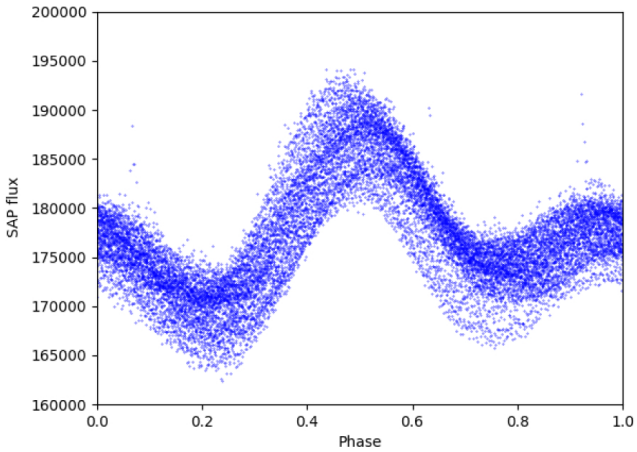

Fig. A.4: TESS sector 27 light curve for AB Dor folded with the binary period of 0.51428 days.

A.3. BD-11 1208: A multi-period star

We finally considered a star with multiple periods, namely, the star BD-11 1208 (Gaia DR3 3009996545138727936 or TIC 201372298), which appears to have received rather little attention so far; according to SIMBAD it is of spectral type A; this is consistent with the *Gaia* color information. In Fig. A.5 we show the first few days of the TESS data obtained in sector 32 of this star, with the inset zooming in on the first 5 hours of this data set, and in Fig. A.6, we show the GLS periodogram for all of the TESS data for BD-11 1208. As shown in Fig. A.6, there are two rather significant periods apparent in the TESS time series, a shorter period of ∼ 1 hour is clearly visible in the modulations in the inset of Fig. A.5, along with a longer period of ∼ 2 days.

It is obvious that the shorter period cannot possibly be a rotation period, it rather appears to be a pulsational period of the A-type star. The longer period could be interpreted as the stellar rotation period, alternatively, it might be the rotational or orbital period, if we interpret BD-11 1208 as a binary system, an interpretation suggested by the large RUWE value derived by *Gaia*. Finally we note that Gaia Collaboration (2023) list this source in their non-single star catalog and quote a period of (2.5427157 ± 0.000097) d with an almost circular orbit for this object. As is clear from Fig. A.6 , the main peak of the GLS periodogram is at 1.987 d, while at the period reported by Gaia Collaboration (2023) merely a minor aliasing peak is located. We further note that the correlation and phase dispersion analyses strongly favor the two day period and conclude that a period of 2.5 d is inconsistent with the TESS photometry. At any rate, BD-11 1208 shows the pitfalls of photometric period analysis.

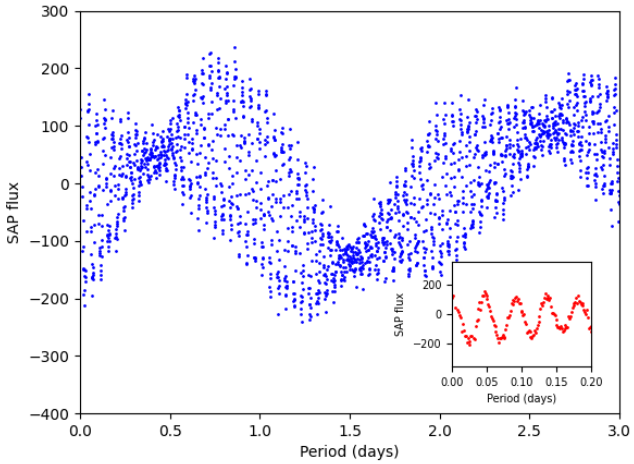

Fig. A.5: TESS sector 32 light curve for BD-11 1208. See text for details.

Appendix B: Period determination procedure

The examples of AV Dor, AB Dor and BD-11 1208 presented in Appendix A demonstrate the difficulties encountered in period determinations in general and especially in active stars. Clearly, the GLS periods (for short-period systems) are very well determined (cf., Figs. A.1 and A.3) and are therefore to be preferred; on the other hand, as shown by the cases of AV Dor and AB Dor, the period associated with the largest GLS power need not necessarily be the correct period, and period aliasing is a well-known and severe problem especially for Fourier-type methods, but also for other period search algorithms. In the cases of AV Dor and

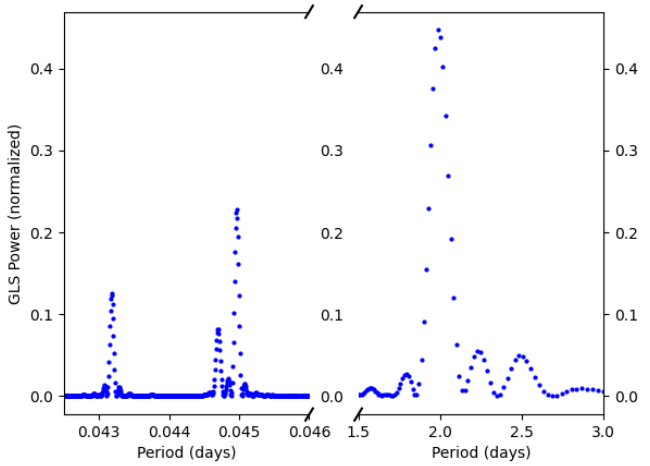

Fig. A.6: GLS periodogram of TESS sector 32 light curve for BD-11 1208. See text for details.

AB Dor, the correct periods are well known and we can properly interpret an apparently "anomalous" light curve as in Fig. A.4; yet if we only had data from TESS sector 27 at our disposal, we would encounter interpretational difficulties. It appears that for active stars the GLS periods appear to be quite trustworthy, yet it is always important to check possible aliasing. We therefore compute for all our periods the values of the autocorrelation correlation function and the Θ statistics to safeguard against aliasing; we do never accept GLS periods with negative values for the autocorrelation function (as is the case for the maximal GLS power in the case of AV Dor), yet we can never be absolutely sure not to be fooled by aliasing effects.

Obviously, short-period systems execute many rotations in a given TESS sector and therefore produce clear and sharp signals in Fourier space as shown in Figs. A.1 and A.3, with the Fourier peaks being much narrower than the peaks found in the autocorrelation function. On the other hand, a low activity star like our Sun with a rotation period of about 25 days would not be detected with our procedures because of the limited sampling period and typically low variability amplitude. Even a moderately active star with a rotation period of, say, 10 days would execute only three rotations in a given TESS sector, which would then naturally lead to much broader signals in the resulting periodograms; also such a period would already come rather close to the instrumental period of 12-13 days.

For these reasons we decided to carry out independent period searches for short and long periods with slightly different procedures, since it is clear that short-period systems need much finer period sampling to accurately determine the peak in a GLS periodogram. In this context, short periods are assumed to be between 0.02 days and 0.6 days. Obviously, a period of 0.02 days is well below the period we would expects for a stellar rotation period and close to or below the break up period, so any period that low cannot be a rotation period. Long periods are then all periods longer than 0.6 days.

As discussed above, for us the GLS period is our method of choice and we search all our sample stars on our period grid for periods with GLS peak power above 0.1; our experience is that true periods typically do reach that value. However, we found it both advantageous and necessary to also consider other period indicators, and in particular, we always demand that the autocorrelation at the peak value exceed 0.1 to be acceptable as a valid period measurement and we always also examine the phased light curves using the phase dispersion minimization approach developed by Stellingwerf (1978).

B.1. Determination of long periods

In our period determination scheme, long periods are periods in the range of 0.6 - ≈ 16 days. As demonstrated in Appendix A.2, we use multiple period determination schemes to reduce the very frequently encountered difficulties by aliasing effects. For the longer periods, fewer and fewer cycles are covered and periods of about 12 days and more are heavily affected by a variety of instrumental effects. We use periodogram, autocorrelation and phase dispersion minimization analysis and illustrate our period search procedures for two TESS light curves, a "good" light curve and a "poor" light curve, respectively.

A "good" light curve and its analysis is shown in Fig. B.1 for the case of TIC 25132999, which refers to the star EXO 040830-7134.7, a dMe star extensively studied already with EXOSAT (van der Woerd et al. 1989). In the left panel of Fig. B.1 we plot (top panel) the TESS SAP flux, which shows a modulated light curve, on top of which there are a number of flares; the data gap after about 13 days is also visible. In middle left panel of Fig. B.1 we show the rectified light curve, used for all period analyses; note that no attempt was undertaken to remove the flares from the recorded light curve. In the right panels of Fig. B.1 we show the analysis results, i.e., the autocorrelation function vs. period (top right panel), the GLS power (medium right panel) and the Θ-statistics of the phase dispersion minimization (bottom right panel). While autocorrelation and phase dispersion show a multitude of peaks, the GLS periodogram shows a single strong peak at a period of 5.18 d, which we interpret as rotation period of TIC 25132999; the GLS best period sine wave corresponding to this period yields a surprisingly good reproduction of the observed light curve, as evidenced in the bottom-left panel of Fig. B.1.

As demonstrated in Fig. B.1, in the specific case of TIC 25132999 both the autocorrelation and phase dispersion curves show a periodic structure, whereas the GLS periodogram yields a single large peak. While it is possible to create circumstances where all of the GLS power is shifted to half the true period (for example, by locating two identical spots 180 degrees apart on the stellar surface as in the case of AB Dor), we argue that in the specific case of the TESS data for TIC 25132999 in TESS sector 2 the GLS period is the correct period which we choose for our further analysis; incidentally, TIC 25132999 is also contained in sector 1 and our period analysis yields identical results.

We next show an example of a "poor" light curve for the case of TESS data for TIC 30311749 obtained in sector 2; incidentally, TIC 30311749 is identical to HD 268670 (K0e, a spectroscopic binary), namely, an active star. In Fig. B.2, we show our analysis of the TESS data for TIC 30311749 in an identical fashion as the TESS data for TIC 25132999 shown in Fig. B.1. The TESS light curve of TIC 25132999 shows the usual gap after about 13 days; furthermore, there are modulations, which are (presumably) in part intrinsic and in part instrumental. The mean levels before and after the 13 days break are different, and the rapid variations near the break are quite odd. The period analysis yields a seemingly significant period near 15 days, which, however, was introduced by our light curve normalization procedures. In addition, the GLS periodogram shows a peak near

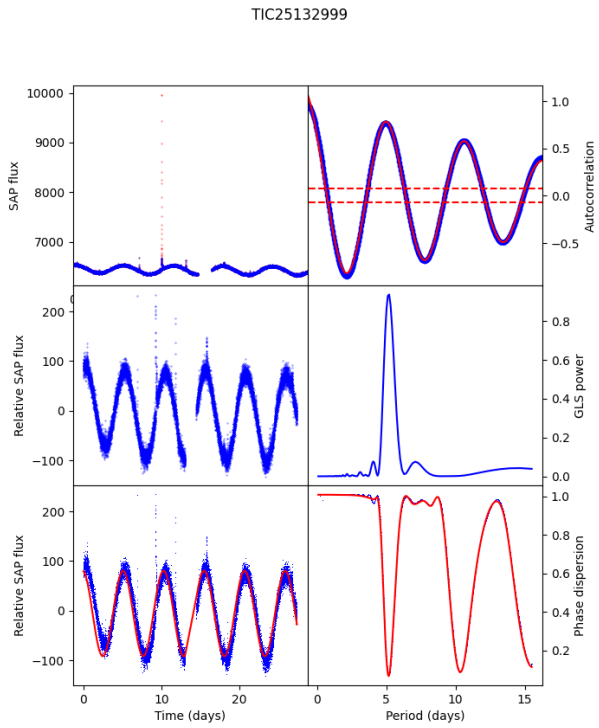

Fig. B.1: TESS light curve analysis for the TESS data (in sector 2) for TIC 25132999. The data are shown in the left panels, the period results in the right panels; see text for details.

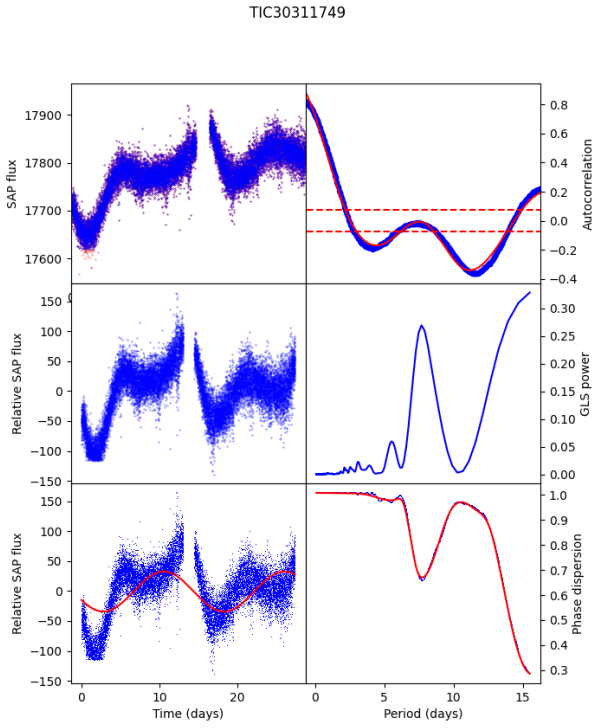

Fig. B.2: TESS light curve analysis for the TESS data (in sector 2) for TIC 30311749. The data are shown in the left panels, the period results in the right panels; see text for details.

8 days with a GLS power of more than 0.25. While we would normally accept periods with such power values and while this value would actually be a reasonable rotation period for an active K dwarf, we cannot recognize a clear autocorrelation signal; therefore, we conclude that in this specific case of TIC 30311749 no trustworthy period assignment can be made on the basis of the available data.

B.2. Determination of short periods

We now turn to the period determination for short periods. Two examples for short period systems with very good light curves have already been produced for the cases of AV Dor (see Fig.A.1) and AB Dor (see Fig. A.3). In the following, we consider a marginal case: that of TIC 126442325, which is identical with the F0V star HD 62707. The results of our period analysis of the TESS data in sector 7 of this source are shown in Fig. B.3 in a fashion completely analogous to Figs. B.1 and B.2. We can recognize from Fig. B.3 a periodicity albeit at rather low levels with a peak-peak amplitude at around the 0.2% level. The main GLS peak at 0.4 days is barely above our cutoff power level at 0.1, the same applies to the autocorrelation value; at twice the period, we can see greater autocorrelation and phase dispersion signals, while the GLS power drops below 0.1.

In the *Gaia* catalog releases, we find a stellar radius of 1.35 $R_{\odot}$ (in DR2) and a spectral broadening velocity v_{broad} = 81.4 ± 2.6 km/s (in DR3) for HD 62707; unfortunately the actual spectra from Radial Velocity Spectrometer (RVS) on board *Gaia* are not available, so no independent analysis can be carried out. If we now interpret v_{broad} as a v sin(i) measurement with $i = 90°$, we find a period of 0.84 days, which would actually reasonably fit to the aliased main GLS peak at 0.4 days. Thus we may actually see the rotational signal of HD 62707 in the TESS data, however, TIC 126442325, does clearly represent a limiting case. The phase dispersion statistics Θ does not show a very clear signal, therefore we refrain from assigning a period to TIC126442325, although the TESS autocorrelation data do suggest some periodicity.

B.3. Final period assignments

In the previous sections we have tried to elucidate the quality range of TESS light curves for the counterparts of eROSITA X-ray sources. Obviously, in the end we have to arrive at a single (hopefully rotation) period for any given star. For each X-ray source, we might have access to period measurements in a given sector (which might possibly be in disagreement) using the three period assessment methods, whereas for a number of sources, we have period measurements in different sectors (for some sources we have coverage in more than 20 sectors); finally, we might encounter successful period measurements both in the long and short period ranges. To deal with this situation, we developed an empirical period classification scheme that assigns a final period and a period quality flag to every star.

As discussed earlier in this work, our period determination scheme is primarily based on the GLS periodogram power (as defined by Zechmeister & Kürster 2009); any successful measurement must yield a GLS power of at least 0.1 and such a measurement is assigned a grade of 1; any maximal GLS power below this value is not considered as successful and is assigned grade 0 and ignored in the following analysis. If a GLS pe-

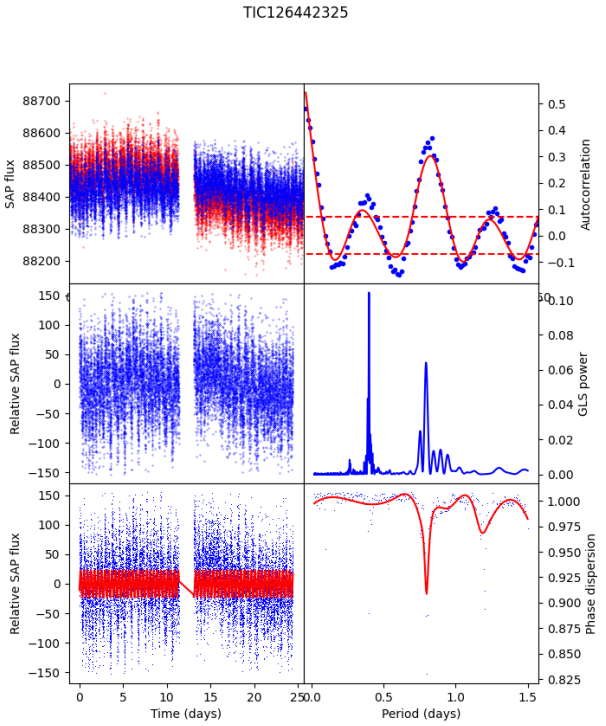

Fig. B.3: TESS light curve analysis for the TESS data (in sector 7) for TIC 126442325. The data are shown in the left panels, the period results in the right panels. See text for details.

riod (with a power above 0.1) is "confirmed" by a measurement of phase dispersion minimization (PDM) and/or autocorrelation (AC) the grade is assigned 2 or 3, if successful period measurements (consistent to within 10%) are available for GLS+PDM and GLS+AC combinations respectively. The best grade assigned to a period derived from data in a single sector, grade 4, requires successful and consistent period determinations (to within 10%) with all the GLS, AC and PDM methods. As described above, this type of analysis was carried out separately for short periods (below 1.6 days) and long periods.

For many of our eRASS1 X-ray sources, we have TESS coverage in more than one sector, however, there are also many sources that were observed by TESS only in a single sector. Clearly, repeated and consistent period determinations in different sectors increase our confidence in the correctness of the period determined for a given star. We therefore increase the grade assignment of consistent period measurements that are available for a given star in several sectors. For sources with successful period measurements in more than one sector available, we first identified the sector with the best period quality and increased the assigned quality grade by 1; if at least three consistent period measurements in different sectors are available; by 2 if between 4 and 8 consistent period measurements in different sectors are available; and by 3, if more than 8 consistent period measurements in different sectors are available. Thus, the maximum possible grade is 7, implying that there are at least nine consistent high quality period measurements available for the given source.

Finally, we needed to merge the short and long period measurements. In the majority of cases (16004), we obtained only a successful long period measurement, in the minority of cases (1106) we obtained only a successful short period measurement, but there are some cases (913) with both long and short period measurements. Almost half of the sources in both categories have periods in the overlap region; namely, the derived periods are consistent with each other. In 116 (out of 913) cases, the derived long period is an alias of the short period and in less than 1% of the cases, the long period is less than 90% of the short period, a clear signature of insufficient period sampling in the GLS calculation. Finally we have 388 remaining cases, where the ratio between the long and short period measurements is often very large; namely, in most cases, due to the fact that a successful short period was determined, while a long period was found near 13.6 days or near 6.25 days, which we interpret as an alias introduced by the TESS data sampling. In these overlapping cases, we therefore adopted the derived short period, except in cases where the long period is an alias of the short period (where we considered the longer period as the more likely one).

In the selected TESS sectors, we analyzed more than 69000 individual TESS light curves, which belong to 22461 different individual sources. For 14004 sources we managed to obtain valid period measurements with grades of 3 and higher; the distribution of the grade quality is shown in Table B.1. Only 11731 of the derived periods have quality assignments greater than 3; that does not imply that the periods for the remaining 2273 sources are wrong, however, the rate of incorrect period determinations among these sources is expected to be higher. An exemplary listing of our results is given in Table 1, the full table is available in the online material.

Table B.1. Quality distribution for successful period determinations.

Period grade	Number
3	2273
4	7542
5	3063
6	670
7	456

Appendix C: A catalog of TESS periods for eROSITA X-ray sources

In the fashion described in Appendix B, we analyzed a total of 65157 individual TESS sector light curves which refer to 18023 unique sources. An exemplary listing of our results is given in Table 1, the full table is available in the online material where we provide a list with all our period determinations, containing TIC number, derived period (in days), the estimated period error (also in days) as well as the grade assigned by us to the respective period determination as well as two flags, the full table is available only electronically.